# TWO DIMENSIONAL NUMERICAL MODELING OF A FLAT HEAT PIPE

**A Thesis Submitted to**
**the Graduate School of Engineering and Science of**
**İzmir Institute of Technology**
**in Partial Fulfillment of the Requirements for the Degree of**

**MASTER OF SCIENCE**

**in Mechanical Engineering**

**by**
**Tümcan ŞEN**

**July, 2014**
**İZMİR**

We approve the thesis of **Tümcan ŞEN**.

**Examining Committee Members:**

**Assist. Prof. Dr. Ünver ÖZKOL**
Department of Mechanical Engineering
İzmir Institute of Technology

**Assoc. Prof. Dr. Moghtada MOBEDİ**
Department of Mechanical Engineering
İzmir Institute of Technology

**Assoc. Prof. Dr. Tahsin BAŞARAN**
Department of Architecture
İzmir Institute of Technology

**9 July 2014**

**Assist. Prof. Dr. Ünver ÖZKOL**
Supervisor, Department of Mechanical Engineering
İzmir Institute of Technology

**Prof. Dr. Metin TANOĞLU**
Head of the Department of
Mechanical Engineering

**Prof. Dr. Tuğrul SENGER**
Dean of the Graduate School of
Engineering and Sciences

# ACKNOWLEDGMENTS

I would like to dedicate this thesis to my family; Mustafa, Nurcan and Çılga Şen, who have been there for me and supported me in every decision that I have made. I would not have become the man I am today if it weren't for them.

I would like to express the deepest appreciation to my thesis supervisor, Dr. Ünver Özkol, for giving me the opportunity to work with him and for his guidance and persistent help throughout my studies.

In addition, I would like to thank Dr. Moghtada Mobedi, who did not turn me down any time I asked for help.

I am thankful to my officemates; Hasan Çelik, Elvan Yıldırım, Eren Uçar and Türküler Özgümüş for giving me the support, courage, joy and help every single day at the office. Thank you for being not just officemates but for being real friends.

I would also like to thank "DTM" lab members; Cenk Kılıçaslan, Ali Kara, Kıvanç Turan and our next-door neighbor, Doğuş Zeren, for their support.

Last but not least, I am very grateful to "Müm" for her endless care, kindness, and support. Thank you for expressing your belief in me any time I feel frustrated. Thank you for not giving up on me and helping me to get over the hard times together. I could not have done it without you.

# ABSTRACT


## TWO DIMENSIONAL NUMERICAL MODELING OF A FLAT HEAT PIPE

In this study, a flat heat pipe with asymmetric boundary conditions is modeled numerically in two-dimensional space. Vapor and wick regions are incorporated in the analysis. The Navier-Stokes equations along with the energy equation are solved under steady state, subsonic, laminar, incompressible and Newtonian flow assumptions. Furthermore, Brinkman-Forchheimer extended Darcy model is employed for the liquid flow in the wick structure. SIMPLE algorithm is employed with staggered grid arrangement to overcome the complications caused by the pressure terms in the momentum equations. The model accounts for uniform injection and suction in the evaporator and condenser sections and it is assumed that evaporation and condensation only occur in evaporator and condenser sections, respectively. Wick structure is presumed to be isotropic and saturated with working fluid. All thermo physical properties are taken as constant and no body forces are included in the model. By considering all of the above information, an in-house code is developed by using the software, MATLAB in order to perform the analysis. The major results introduced are the distribution of velocity components along with their profiles at different locations, temperature distribution and pressure drops along the heat pipe as well as their distributions within the domain. Additionally, parametric analyses are performed to investigate the effects of heat input and heat pipe aspect ratio on the required capillary pressure.

# ÖZET

## DÜZLEMSEL BİR ISI BORUSUNUN İKİ BOYUTLU NÜMERİK MODELLENMESİ

Bu çalışmada asimetrik sınır şartlarına sahip düzlemsel bir ısı borusu iki boyutlu düzlemde numerik olarak modellenmiştir. Analize buhar ve sıvı fazları dahil edilmiştir. Navier-Stokes denklemleri ve buna ek olarak enerji denklemi çözülmüştür. Denklemler çözülürken akışkan; denge durumunda, sabsonik, lamıner, sıkışmayan ve Newton akışkanı olarak varsayılmıştır. Gözenekli yapı içerisindeki sıvı faz Darcy denkleminin Brinkman-Forchheimer tarafından geliştirilen versiyonu ile modellenmiştir. Momentum denklemlerindeki basınç terimlerinin neden olduğu sorunları önlemek için kontrol hacim sıralı nodlarla bölünmüş ve SIMPLE algoritması kullanılarak denklemler çözülmüştür. Modelde, evaporatör ve kondansörde üniform vakum ve emme mekanizması olduğu, buharlaşmanın yalnızca evaporatorde ve yoğuşmanın yalnızca kondansörde gerçekleştiği kabul edilmiştir. Gözenekli yapının izotropik ve çalışma sıvısına doymuş bir şekilde olduğu varsayılmıştır. Ayrıca modelde kullanılan bütün termo-fiziksel özellikler sabit kabul edilip, cisme etki eden kuvvetler çözümlere dahil edilmemiştir. Bütün bu varsayımlar göz önünde bulundurulup, MATLAB yazılımı kullanılarak gerekli analizleri yapabilecek bir kod geliştirilmiştir. Hızın ısı borusu içindeki dağılımı ve belli bölgelerdeki hız profilleri, sıcaklık dağılımı ve ısı borusu içindeki basınç kayıpları ve bu kayıpların dağılımı sunulan başlıca sonuçlar arasındadır. Bunlara ek olarak ısı girdisinin ve ısı borusunun boy-en oranının gerekli olan kapiler basınç üzerindeki etkisi parametrik olarak incelenmiştir.

# TABLE OF CONTENTS

# LIST OF FIGURES

# LIST OF TABLES

# LIST OF SYMBOLS

| | | |
|---|---|---|
| a | Coefficient of the transported variable | - |
| A | Area | $m^2$ |
| b | Source term | m |
| C.V. | Control Volume | - |
| $C_E$ | Ergun's coefficient | - |
| $C_P$ | Specific heat | kJ/kg K |
| D | Diffusion conductance flux | kg/s |
| F | Convective mass flux | kg/s |
| g | Gravity | $m/s^2$ |
| $h_{fg}$ | Latent heat of evaporation | kJ/kg |
| k | Thermal conductivity | W/m K |
| K | Permeability | - |
| L | Length | m |
| n | Unit vector | - |
| P | Pressure, Nodal point | Pa, - |
| q | Heat flux | $W/m^2$ |
| R | Gas constant, Residual | kJ/kg K, - |
| s | Entropy | kJ/kg K |
| S | Source term | - |
| T | Temperature | K |
| u | Velocity in x-direction | m/s |
| v | Velocity in y-direction | m/s |
| V | Volume | $m^3$ |
| x | Axial direction | - |
| y | Transverse direction | - |

**Greek Symbols**

| | | |
|---|---|---|
| α | Relaxation | - |
| Γ | Diffusion Coefficient | - |
| δ | Difference | - |
| Δ | Difference | - |
| ε | Porosity | - |

| | | |
|---|---|---|
| $\Theta$ | Thermo physical properties group | $m^2$ |
| $\mu$ | Dynamic viscosity | N $s/m^2$ |
| $\rho$ | Gravity | $m/s^2$ |
| $\phi$ | Geometric dimensions group | $m^2$ |
| $\psi$ | Dimensionless number ($\phi/\Theta$) | - |

**Subscripts**

| | |
|---|---|
| a | Adiabatic section |
| c | Condenser |
| e | Evaporator |
| E | East nodal point |
| e | East cell face |
| eff | Effective |
| in | Inlet |
| int | Interface |
| l | Liquid |
| N | North nodal point |
| n | North cell face |
| nb | Neighbor |
| out | Outlet |
| p | Dependent |
| s | Solid |
| S | South nodal point |
| s | South cell face |
| sat | Saturation |
| u | Independent |
| v | Vapor |
| W | West nodal point |
| w | West cell face |

**Dimensionless numbers**

| | | |
|---|---|---|
| Pe | Peclet Number | - |
| Re | Reynolds Number | - |

**Superscripts**

| | | |
|---|---|---|
| - | Average | |
| ' | Correction | - |
| * | Guessed | - |

# CHAPTER 1

# INTRODUCTION

Heat pipes are passive heat transfer devices, which are used to transport heat over a distance with high thermal conductivity. They have been becoming more popular throughout the years over to the other conventional heat transfer methods. Out of many superiorities of a heat pipe, the capability of transporting significant amount of heat with minimal temperature differences takes them a step further. Moreover, no additional power requirement and various design options such as one-way heat transfer are some of other advantages of heat pipes.

The concept dates back to 19$^{th}$ century, when Perkins family offered the first implementation of passive heat transfer with high thermal conductance: the "Perkins tube". Perkins tubes transported heat by the latent heat of evaporation process of the fluid and generally used gravitational force to complete the cycle. However, the closest design of today's heat pipes was proposed by Jacob Perkins (Perkins, 1836). This prototype was a sealed tube in which small amount of water was circulated in two phases.

The heat pipe itself was first proposed and patented by Gaugler of General Motors (Gaugler, 1944). For return mechanism, instead of gravitational force, Gaugler suggested a wick structure that is made of sintered iron. The capillary pressure difference, created by the wick structure, drove the condensed fluid back to the evaporator regardless of the orientation of the heat pipe. However, General Motors did not use and develop this idea.

In 1963, the idea of heat pipe came up again and capillary-based heat pipes were both developed and patented by Grover on behalf of U.S. Atomic Energy Commission (Grover, 1966). In this patent application, Grover emphasized the importance of heat pipe by stating " With certain limitations on the manner of use, a heat pipe may be regarded as a synergistic engineering structure which is equivalent to a material having a thermal conductivity greatly exceeding that of any known metal" (Grover, 1966). Grover presented limited theoretical but mostly experimental results, which had been

conducted with stainless steel heat pipes that had screen type wick structure and various types of working fluid inside, namely lithium, silver and sodium.

After preliminary theoretical results were proposed by Cotter (1965), worldwide research on heat pipes began, first by the United Kingdom Atomic Energy Laboratory at Harwell where experimental work on sodium heat pipes were carried out, then by Joint Nuclear Research Center in Ispra, Italy where similar heat pipe analyses were performed. Soon after, Germany, France and the USSR also did some introductory studies.

Introduction of heat pipes to commercial area was first commissioned by RCA (Judge, 1966; Leefer, 1966). During a two-year period between 1964 and 1966, the U.S. government supported the research. Various materials including copper, nickel and glass were used in the wall structure of heat pipes where water, sodium, lithium and cesium were used as working fluid. Experiments were conducted and an operating temperature of 1650°C had been accomplished.

## 1.1. Principles of Operation

Heat pipes are simply evacuated tubes that contain small amount of fluid and consist of evaporator, adiabatic and condenser sections, respectively. The heat transfer through the heat pipe is achieved by latent heat of evaporation process of fluid in the evaporator section. When heat is applied to the evaporator through external sources, the working fluid vaporizes and the increasing vapor pressure due to vaporization drives the vapor to the condenser through adiabatic section. In the condenser section, vapor condenses while releasing latent heat to the heat sink. The condensate is then carried back to the evaporator section by means of various ways.

In Figure 1.1, a schematic of a heat pipe, which uses capillary pressure, one of the various return mechanism of the condensate mentioned above, is presented. In order to obtain capillary pressure, a wick structure is fabricated inside the heat pipe with different manufacturing techniques. As can be seen in the figure, liquid meniscus at the intersection of vapor and liquid flow is formed with different curvatures depending on the location. The reason behind the curvatures is the surface tension of the liquid caused by the porosity of the wick structure. The condensation process in the condenser section results in a less curved menisci, while highly curved menisci are generated in the

evaporator section due to the withdrawal of liquid into the pores. The resulting pressure difference is called capillary pressure and the condensate is driven back to the evaporator by means of this force. Hence, the heat pipe is able to work regardless of its orientation with respect to the ground as long as the capillary pressure compensates the liquid and vapor pressure losses, and adverse body forces. This kind of mechanism is almost the same as water being sucked from the ground by the root of a tree and transported to the every single branch despite of the gravitation.

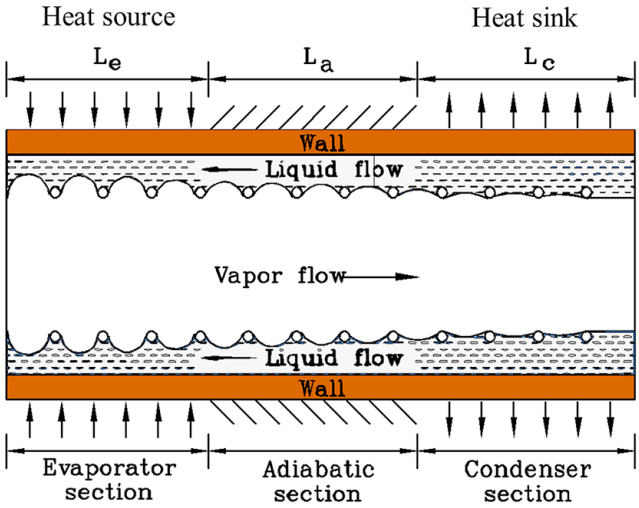


Figure 1.1. Schematic of a conventional heat pipe
(Source: Faghri, 2012)

In order for a heat pipe to operate, the capillary pressure generated by the wick structure should be higher than the vapor& liquid pressure drops and adverse gravity force, if exists. Otherwise, enough liquid cannot be supplied to the evaporator and this eventually leads to dry-out condition, which halts the heat pipe operation. Axial variation of pressure at the liquid-vapor interface in a heat pipe is presented in Figure 1.2. $L_e$, $L_a$ and $L_c$ represent the lengths of evaporator, adiabatic and condenser regions, respectively. The causes of pressure drop in vapor region are friction, inertia and evaporation & condensation effects while the reason for pressure drop of liquid is due to frictional force, which originates in the pores of wick structure.

Both the effects of “no gravity force” and “adverse gravity force” are shown in Figure 1.2. If the gravity is against the liquid flow direction, liquid pressure drops further. In such a case, the capillary pressure should be even higher than the pressure value of “no gravity force” assumption because it is supposed to cover this loss, too, in order to prevent dry-out in the evaporator. Furthermore, the pressure values of vapor

and liquid phases are equal to each other at the condenser end cap as a result of flat interface, as can be observed in Figure 1.1. On the other hand, a maximum pressure difference occurs at the evaporator end cap and equals to the sum of all losses in the pipe, which is named a capillary pressure difference.

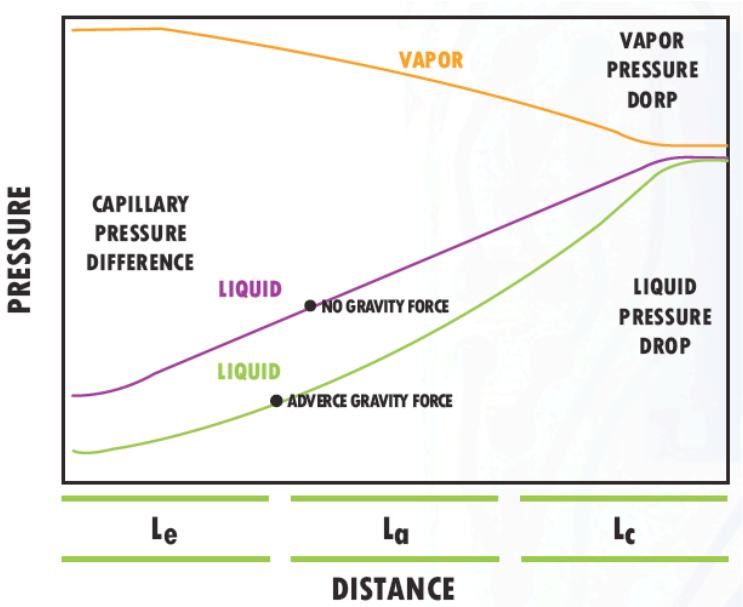


Figure 1.2. Axial variations of liquid and vapor pressures at liquid-vapor interface (Source: Faghri, 1995)

The aim of current study is to model a heat pipe mathematically in terms of hydrodynamic and heat transfer processes. Thus, thermal processes occurring inside the heat pipe should also be investigated in addition to the pressure distribution in the heat pipe. Figure 1.3 represents the schematic of heat pipe operation and Figure 1.4 visualizes the thermodynamic cycle of a typical heat pipe on temperature vs. entropy (T-s) diagram. As the numbers indicate in the figures, the compressed liquid is heated by a heat source, to saturated vapor (1-2). Resulting pressure difference between evaporator and condenser drives the vapor to condenser through adiabatic section (2-3). The vapor is almost isothermal throughout the adiabatic section until it reaches to condenser. Here, the vapor is again condensed to compressed-liquid while releasing heat to the sink (3-4) and carried back to the evaporator by means of capillary force (4-1). One fact should be emphasized at this point, though: Most heat pipes have very small temperature differences between their end caps. This difference is zero for an ideal heat pipe. However, it violates the second law of thermodynamics and does not represent the real life conditions.

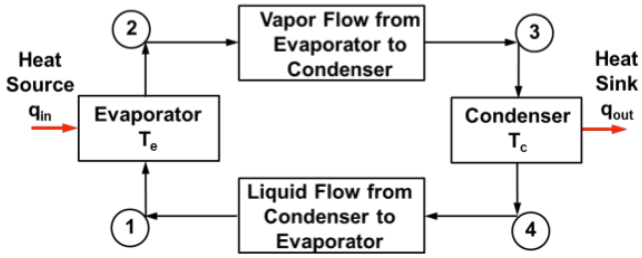


Figure 1.3. Schematic of heat pipe operation
(Source: Peterson, 1994)

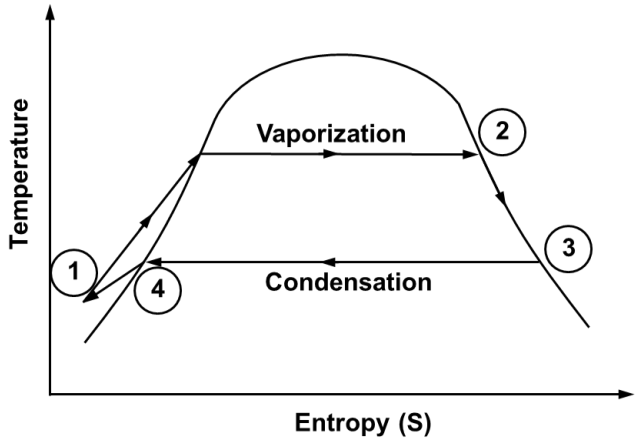


Figure 1.4. Thermodynamic cycle of a heat pipe
(Source: Peterson, 1994)

## 1.2. Types of Heat Pipe

All heat pipes work in two-phase cycle where evaporation and condensation processes occur at evaporator and condenser sections, respectively. Most heat pipes have adiabatic section that separates those two sections from each other.

In section 1.1, a conventional heat pipe (capillary-driven heat pipe), which makes use of wick structure as return mechanism, was introduced. Moreover, single heat source and heat sink were assumed for the sake of simplicity. However, heat pipes can have multiple heat sources and heat sinks; or many other forces besides capillary pressure force can be utilized for return mechanism such as gravitational, centrifugal, electrostatic and osmotic forces.

In order to satisfy the demand in the market, heat pipes with different dimensions, shapes and orientations exist. According to the place of use, appropriate heat pipes can be manufactured from a wide range of options to gain the highest possible outcome. Different kinds of heat pipes are introduced below.

### 1.2.1. Two-phase Closed Thermosyphon

Thermosyphons are the predecessors of today's heat pipes. They work in a two-phase cycle and are composed of evaporator, adiabatic and condenser sections. In fact, Thermosyphons are wickless gravity-assisted heat pipes unlike conventional heat pipes, which use wick structure as return mechanism. The thermosyphon should be placed such that the evaporator is located below the condenser in order for condensate to flow down to the evaporator by means of gravity force. Figure 1.5 shows the working principle of a thermosyphon visually.

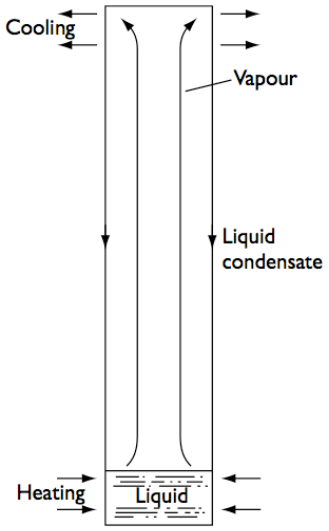


Figure 1.5. Two-phase closed thermosyphon
(Source: Reay & Kew, 2006)

### 1.2.2. Variable Conductance Heat Pipe

These types of heat pipes are also called as gas-loaded or gas controlled heat pipes. They are used when precise and reliable temperature control is needed. The advantage of employing gas-loaded heat pipes is to control and keep the evaporator wall temperature constant by changing the condenser area no matter how much heat is applied to evaporator. In order to perform such an operation, non-condensable gas (NCG) is introduced to the heat pipe and it is swept to the reservoir, which is mounted to end of the condenser as can be seen in Figure 1.6.

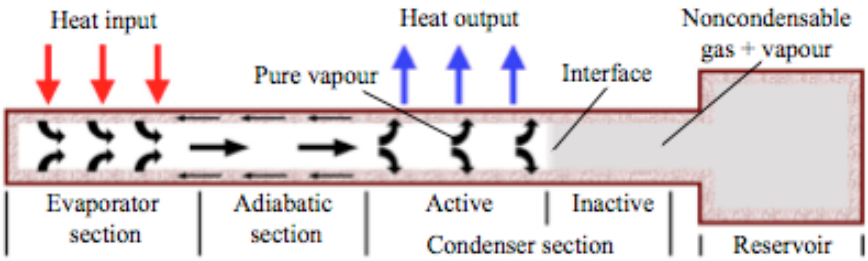


Figure 1.6. Schematic of gas-loaded heat pipe
(Source: Cleary et al., 2013)

Variable conductance heat pipe involves a NCG reservoir in addition to the basic sections of a heat pipe. The working fluid in the condenser and NCG in the reservoir create an immiscible interface that moves axially along the condenser section to change the condenser area. When the ambient temperature is elevated, operating temperature of heat pipe increases which results in a rise in the operating pressure. This pressure gain causes NCG to be compressed, thus, the condenser area to be expanded. The broader the condenser area is, the higher the heat output is obtained. Higher heat output results in the compensation of the increased heat input and a constant temperature value is achieved on the evaporator wall.

### 1.2.3. Loop Heat Pipe

Loop heat pipes are also passive heat transfer devices, which are very similar to the conventional heat pipes. What differs them from the conventional heat pipes is the separate liquid and vapor lines that are co-current as shown in Figure 1.7. Loop heat pipes are mostly used to transfer heat over long distances with no additional power input given to the system.

Heat applied to the evaporator component vaporizes the working fluid in the compensation chamber and the vapor reaches to the condenser section through vapor line. In condenser, the vapor is condensed and travels to the compensation chamber back where liquid is stored. The wick structure separates the liquid phase in the compensation chamber and vapor phase in the vapor removal channel.

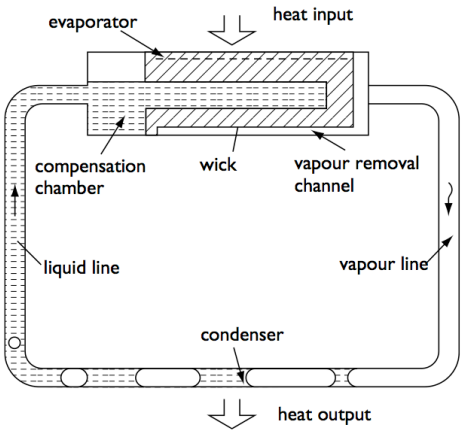


Figure 1.7. Loop heat pipe
(Source: Reay & Kew, 2006)

## 1.2.4. Pulsating Heat Pipe

Pulsating heat pipes are composed of a serpentine tube of capillary diameter. The reason for using capillary diameter is to make use of surface tension of fluids and create a slug-plug motion for cycling mechanism. Pulsating heat pipes have both closed and open configurations.

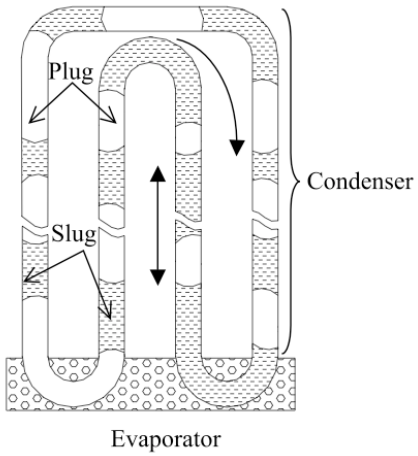


Figure 1.8. Closed loop pulsating heat pipe
(Source: Tong, Wong, & Ooi, 2001)

The serpentine tube is evacuated, and then filled with working fluid consisting of slug of liquid and vapor bubbles, which is illustrated in Figure 1.8. As heat is applied to the evaporator and temperature rises, the vapor bubbles grows and liquid moves. The bubbles, which reach to the condenser, shrink and the cycle continues by means of this grow and shrink mechanism.

## 1.2.5. Rotating Heat Pipe

Rotating heat pipes are conical shaped heat pipes whose condensers have a smaller radius than their evaporator sections as presented in Figure 1.9.

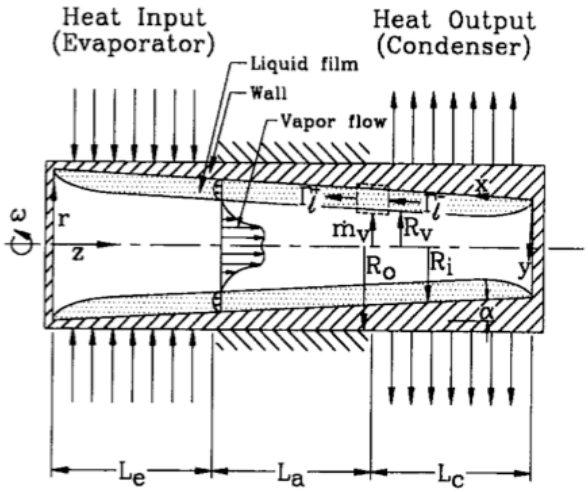


Figure 1.9. Rotating heat pipe
(Source: Harley & Faghri, 1995)

They operate in the same manner like conventional heat pipes do. The only difference is the return mechanism of condensed liquid: The condensate travels back to the evaporator by means of the shape of heat pipe and centrifugal force.

## 1.2.6. Flat Heat Pipe

Flat heat pipes are rectangular shaped heat pipes with a small aspect (i.e. height to length) ratio. As in most heat pipes, wick structure is utilized for return mechanism of the condensate. They are broadly used in electronic cooling applications and many different variations can be manufactured to meet the necessary specifications. A basic type of a flat heat pipe is presented in Figure 1.10 with all of its components indicated.

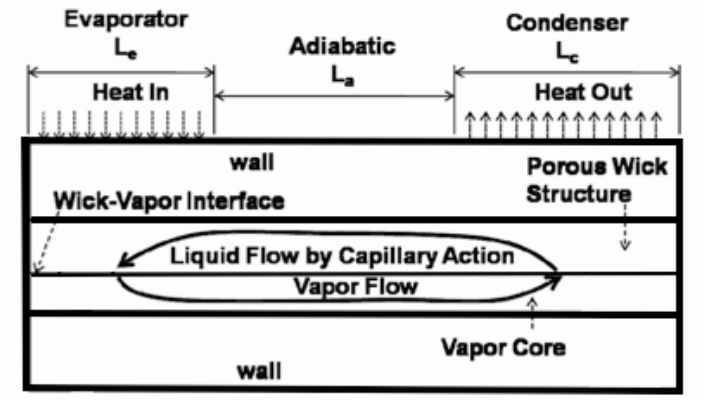


Figure 1.10. Flat heat pipe
(Source: Ranjan, Murthy, Garimella, & Vadakkan, 2011)

Working principle of flat heat pipes is the same as conventional heat pipes. Heat is applied to the evaporator and released to the heat sink in the condenser. Adiabatic section separates those two sections and condensate is carried back to the evaporator by means of capillary pressure created by the wick structure.

## 1.3. Operational Limitations of Heat Pipe

Although heat pipes are able to transport huge amount of heat compared to the other conventional methods, there are some certain parameters that restrain the maximum heat transfer capability of heat pipes. These parameters depend on the type of fluid used, wick structure; and the size, shape and material of the heat pipe. Capillary, viscous, entrainment, sonic and boiling limits are the most basic limitations that are encountered and are not to be passed during the operation of heat pipes. Figure 1.11 displays the operational limitations of a heat pipe on an axial heat flux versus temperature graph. As long as working conditions of heat pipe stay in the area enclosed by these limits, heat pipes can function properly for heat transfer applications. The aim of this study is to initiate a model that predicts the necessary conditions in order to keep the heat pipe operational characteristics within the working limits.

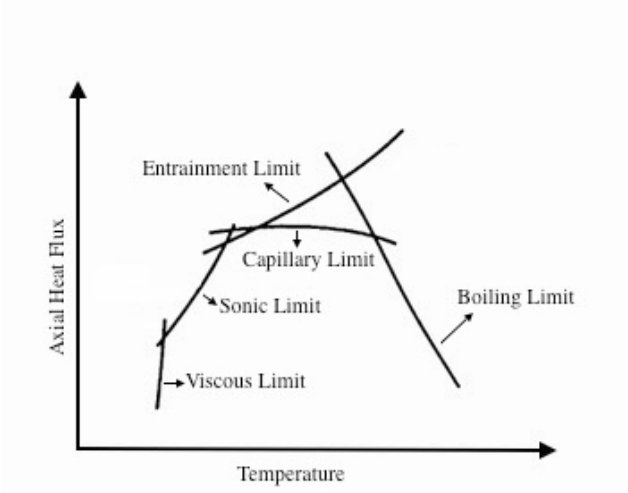


Figure 1.11. Operational Limitations of Heat Pipe

### 1.3.1. Capillary Limit

Wick structure of heat pipe provides the return mechanism of condensed fluid back to the evaporator by using capillary pressure created by the meniscus level differences of condenser and evaporator sections at the vapor-wick interface. Maximum capillary pressure that a wick can sustain depends on the type of fluid and material used for the wick structure. As long as enough capillary pressure is provided, which overcomes the vapor pressure drop, liquid pressure drop and gravitation/body force pressure drop, sufficient condensed fluid is pumped to the evaporator and heat pipe can function properly. Any capillary pressure value lower than those three main pressure losses causes heat pipe evaporator to dry out and a sudden increase in the wall of evaporator section occurs. Capillary limit is frequently encountered and usually determines the limiting performance of a heat pipe.

### 1.3.2. Viscous Limit

Viscous limit occurs at low operating temperatures when enough pressure difference between the end caps cannot be achieved to compensate pressure loss of vapor due to viscous forces. In this case, the vapor transport to condenser section is interrupted and consequently, enough condensate in the condenser cannot be obtained. Viscous limit can also be called as vapor pressure limit.

### 1.3.3. Entrainment Limit

In most of heat pipes, vapor and liquid phases flow in opposite directions. In low operating temperature heat pipes with small diameter or high operating temperature heat pipes with large heat input; high shear force occurs at the vapor-wick interface caused by high relative velocity between liquid and vapor flows. The excessive shear force may result in some fluid particles to be entrained into the vapor flow and carried back to the condenser before arriving to the evaporator. If the entrainment is too much, insufficient amount of liquid reaches to the evaporator and dry-out may take place in the evaporator. This type of limit is named as the entrainment limit.

### 1.3.4. Sonic Limit

Sonic limit is very similar to the chocked flow case in converging-diverging nozzles. In heat pipes, the velocity of vapor flow reaches to its maximum value at the end of evaporator, which corresponds to the throat of converging-diverging nozzle. As known, chocked flow occurs when the local speed of sound is exceeded at the throat of nozzle. Similarly, when vapor velocity takes a higher value than the local speed of sound at the end of evaporator section, sonic limit is reached and vapor flow is inhibited. However, increasing the evaporator temperature can result in a higher sonic limit value so it does not represent a serious failure as other limits.

### 1.3.5. Boiling Limit

When high heat flux is applied to evaporator, nucleate boiling occurs in the wick structure of the evaporator section and this makes vapor bubbles to be formed. Vapor bubbles prevent the liquid flow from arriving to the evaporator section. If the boiling continues, evaporator dries out and extensive temperature values at the evaporator wall are reached.

## 1.4. Disadvantages of Heat Pipe

Even though heat pipes are very effective devices in heat transfer, there are some difficulties associated with the design and material selections depending on the types of the heat pipes.

Since the heat pipes contain small amount of working fluid, selection of the working fluid is actually a crucial step in heat pipe design. The working fluid should be chosen so that it is able to evaporate and condensate at the predefined operating temperature. Otherwise, the heat pipe will not work considering that the heat transfer is achieved by latent heat of evaporation process. Furthermore, the working fluid should also be compatible with the wick structure and container materials. In some cases, the working fluid may undergo a chemical reaction with the wick and container material and the heat pipe may be damaged (Peterson, 1994).

The heat pipes are also preferred for cooling purposes of the electronic devices and leakage may cause hazardous results in these kinds of devices. That is why the sealing of the heat pipe container is one the major processes during heat pipe manufacturing. Moreover, the container material should be selected carefully in order to resist the external corrosion of the heat pipe container (Peterson, 1994).

Another important design criterion in heat pipes is the material, production techniques and the porosity of the wick structure. Manufacturing of the wick structure may cost a lot depending on the desired capillary pressure values. The capillary pressure supplied by the wick structure is highly dependent on the porosity and the degree of porosity should be determined accordingly.

As indicated in the previous sections, there are many heat pipe types with various designs depending on the area of use. For some designs, the heat pipe structure may be complex and large storage volumes may be required. Additionally, the some types of heat pipe may involve moving parts and these kinds of heat pipes should be design more carefully and higher production costs may be required in these cases (Reay & Kew, 2006).

## 1.5. Literature Survey

Due to both higher costs and longer time periods of performing experiments, theoretical modeling is mostly preferred as a preliminary stage because of its being a relatively simple, quick and cheaper way of modeling when suitability of a product is under concern. However, modeling does not always represent all of the real life conditions because of their complexities and difficulties that are very hard incorporate into the virtual environment. Instead, some simplifications and assumptions are made to satisfy the real life conditions as much as possible and predict reasonable estimations.

Even though heat pipes have many advantages over the conventional heat transfer methods, choosing the proper heat pipe structure, material, type and size is actually a very crucial process in order to make use of the heat pipe in a most effective way. At this point, modeling steps in and helps the researcher to decide on the most appropriate heat pipe with the right parameters.

As stated above, some difficulties in explaining the real-life conditions are encountered during modeling and the researchers have performed many studies to overcome these difficulties. Up until now, the effects of heat pipe wall thickness and conductivity along with the gravity and wick porosity are all examined. In addition, the effects of multiple heat sources and changing heat source strength on the heat pipe performance were included in some of the analyses. The effects of using different types of materials on the heat pipe limitations and performance also drew attention of some researchers. With all these considered, great effort has been spent to model the vapor-liquid interface, the liquid flow inside the wick structure and the vapor flow. Some of the basic studies, which have been conducted so far, shall be investigated in this section.

The vapor flow in a flat heat pipe with both symmetric and asymmetric boundary conditions was investigated numerically by Ooijen and Hoogendoorn (1979) and validated by the experiments. Finite difference method with hybrid scheme was used in order to solve the continuity and momentum equations. The study aimed to determine the validity of Poiseuille flow approximation for the vapor flow in a flat heat pipe. Different Reynolds numbers, increasing from 1 to 50, were used for parametric study. The velocity and pressure profiles were obtained and it was concluded that computed pressure drops had almost the same value as assumed by Poiseuille flow approximation for symmetric boundary condition with $Re \leq 25$. On the other hand, for the asymmetrical case, the computed pressure drop over the heat pipe was a lot higher

than the pressure drop found by Poiseuille flow model. The underlying reason for this result was due to the fact that an enormous increase in the wall shear stress occurred in the condenser section caused by the recirculating flow zone formation in this section for Re≥ 10. In such case, the model was not valid for vapor flow. However, the recirculating flow zone could be impeded by the suction boundaries for symmetrical case and the model could be applied to the vapor flow calculations.

Vafai & Wang (1992) and Zhu & Vafai (1996) utilized pseudo-three-dimensional analytical model in their studies to solve vapor and liquid flows of an asymmetrical flat heat pipe and asymmetrical disk-shaped heat pipe, respectively. The Darcy's law was applied to the fluid flow in the wick by Vafai & Wang (1992) and the applicability of a flat heat pipe as a heat sink for Boron Neutron Capture Therapy[1] was examined. Vapor velocity on x-y plane, axial pressure distribution in vapor and liquid phase and axial temperature profile of vapor flow were presented in their results. Zhu & Vafai (1996), however, employed non-Darcian transport through wick region which includes the effects of boundary and inertial forces. Hydrodynamic coupling of liquid and vapor flow as well as the gravitational effects was integrated in their work. The effect of vertical wick columns was also analyzed. The results indicated that the implementation of Darcy's law rather than non-Darcian transport within the wick structure leads to considerable errors in liquid flow rate, maximum heat transfer capability and pressure drop calculations. In addition, omitting the effects of hydrodynamic coupling of liquid and vapor flow and same flow rate assumption in the top and bottom wicks cause errors in the flow simulations.

Another study which employed non-Darcian transport through wick structure was conducted by Zhu & Vafai (1999) for low-temperature cylindrical heat pipes. The hydrodynamic coupling between liquid and vapor flow was also incorporated in the work and a closed-formed solution was obtained analytically with convective cooling boundary condition in the condenser section The vapor and liquid velocity, vapor and wall temperatures and pressure distribution were determined as well as the capillary limit of the heat pipe during steady state operation. It was concluded that the effects of hydrodynamic coupling in the interface does not have a significant impact on low-temperature heat pipes. However, the Darcy's law assumption for the porous medium in

[1] A method for treatment of brain tumors

the wick region causes critical errors in simulating the flow and determining the maximum heat transfer capability of the heat pipe.

In the analysis carried out by Zuo & Faghri (1998), the heat pipe components were considered as thermal resistances of a network system as illustrated in Figure 1.12. Each number symbolizes an operation, which is considered as the resistance of a network system. The system aimed to model transient behavior of a heat pipe. The complexity of governing equations was reduced and solved as 1st order linear ordinary differential equations by using the Runge-Kutta method.

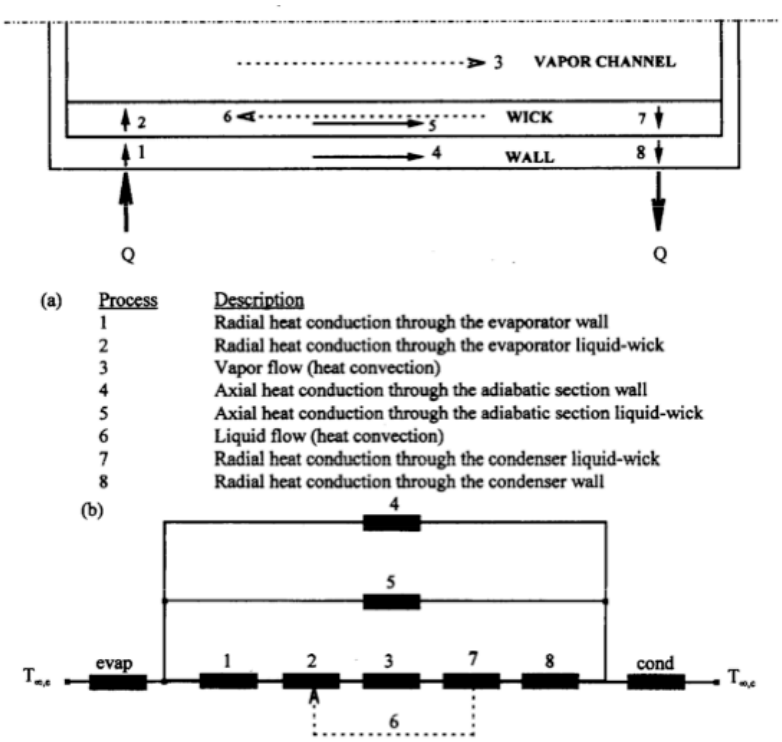


Figure 1.12. Heat pipe components as a network analogy
(Source: Zuo & Faghri, 1998)

At the end of the study, a dimensionless number ($\psi=\phi/\Theta$) was proposed as the ratio of geometric dimensions and thermo physical properties of the working fluid along with the heat pipe wall material. According to the writers, the proper operation condition of the heat pipe depends on this ratio and if $\psi>1$, this condition is satisfied. Otherwise, the heat pipe cannot operate correctly.

The effects of vertical wick, evaporative heat input and the size of heat pipe on the capillary limit and thermal resistance were analyzed by Xiao & Faghri (2008). For this purpose, a three-dimensional model was developed and the equations of heat conduction in the wall, vapor flow and wick region along with liquid-vapor interface

were solved numerically by using finite volume method for the discretization of the equations. Figure 1.13 shows the pressure drop and liquid velocity along the x-direction for heat pipes with/without vertical wick columns in the vapor chamber. The results predict that the addition of vertical wick columns on the vapor chamber improves the capillary limit and thermal resistance within the heat pipe due to the increase in velocities and pressure drop within the heat pipe as can be derived from the figure, because vertical wick columns enhance the return mechanism for the liquid flow. It was also shown that velocities of liquid and vapor flow, pressure drop and the interface velocity increased with elevated heat input values and larger heat pipe sizes had favorable effects on the thermal performance of the heat pipe.

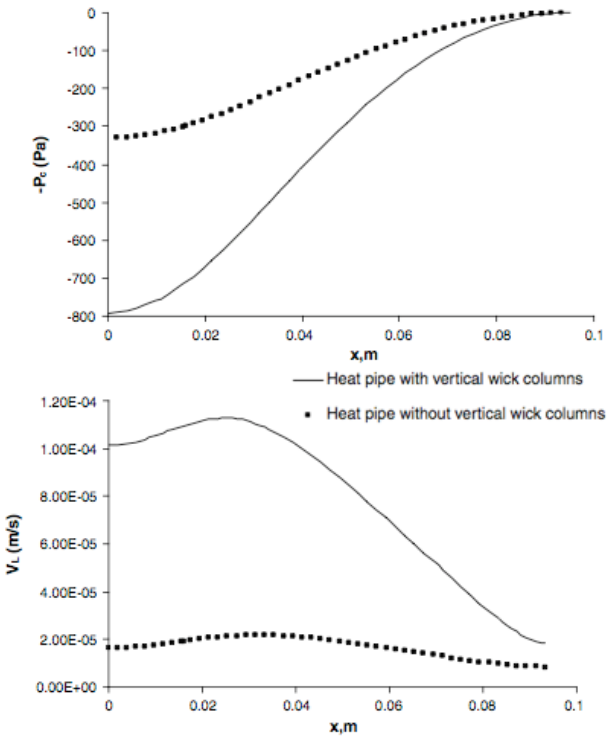


Figure 1.13. The effect of vertical wick columns on liquid velocity and pressure drop (Source: Xiao & Faghri, 2008)

Chen, Zhang, Shi, Wu and Peterson (2009) suggested a "Ω"-shaped micro groove for the return mechanism of liquid flow, as illustrated in Figure 1.14. A numerical analysis was made to obtain heat pipe performance and the maximum heat transfer capability.

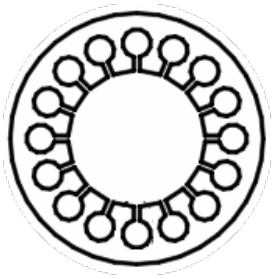

Figure 1.14. Cross section of a "Ω"-shaped micro grooved heat pipe
(Source: Chen et al., 2009)

In the study, wick-vapor interface was investigated carefully. For this purpose, the effects of liquid-vapor interfacial shear stress, variation of meniscus radius and contact angle at the interface were also incorporated in the theoretical model. The results revealed that minimum meniscus radius at the evaporator section is to be formed to obtain maximum heat transport within the heat pipe. Furthermore, "Ω"-shaped groove decreases the effect of vapor on the liquid flow due to smaller contact area, thus, improves the capillary pumping force. Another parameter that has a favorable effect on the capillary pumping is smaller wick slot width. However as the wick slot width gets smaller, friction loss within the groove increases. Lastly, larger wick diameter enhances the permeability of the groove while decreasing the effective thermal conductivity.

In addition, many researchers analyzed the effect of axial conduction in the wall on the heat pipe performance. Sobhan, Garimella and Unnikrishnan (2000) worked on two-dimensional space for heat pipe modeling while Hung & Tio (2010) and Shabgard & Faghri (2011) made use of analytical methods to perform one-dimensional and two-dimensional modeling, respectively. Equations of liquid and vapor flows along with the heat conduction equation in the wall were solved in these three studies. The common conclusion of the studies is that neglecting wall conduction in the heat pipe simulations can cause significant errors in velocity and pressure drop calculations unless the conductivity and thickness of heat pipe wall is very small. Sobhan et al. (2000) and Hung & Tio (2010) indicated that evaporation and condensation can also take place in the, so called, adiabatic section of the heat pipe if the conductivity and thickness of wall are large enough to carry the heat flow axially. Consequently, the velocity distributions, thus, the heat pipe performance are effected by the axial conduction in the heat pipe wall. Shabgard and Faghri (2011) also examined the case when the heat pipe evaporator was subjected to multiple heat sources and when the condenser wall experienced either constant heat flux or convective cooling.

Vadakkan, Garimella, & Murthy (2004) and Aghvami & Faghri (2011) also studied the effects of wall conductivity on the heat pipe performance. However, the main issue in their studies was to monitor the heat pipe performance when exposed to different heating and cooling configurations. Vadakkan et al. (2004) worked on flat heat pipes which were subjected to multiple heat source and the effects of heat source strength and separation were determined as well as the location of dry-out and maximum pore radius that could sustain necessary pressure drop within the heat pipe. Three-dimensional continuity, Navier-Stokes and energy equations along with the conduction in the wall were solved numerically by using semi-implicit method for pressure linked equations (SIMPLE). The results showed that location of dry-out point deviated from the point of maximum temperature. Moreover, as the distance between heat sources increased, maximum temperature in the heat pipe decreased which led to lower liquid and vapor pressure drops as illustrated in Figure 1.15.

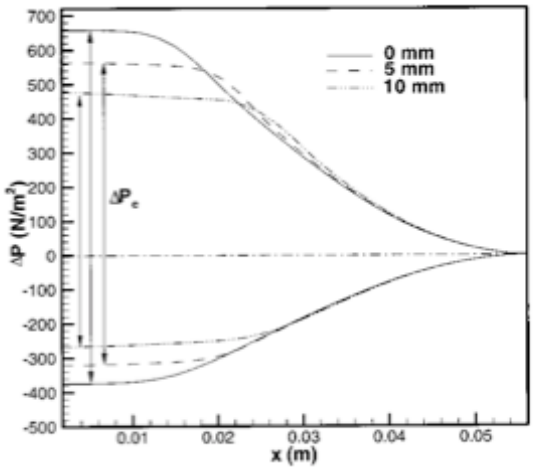


Figure 1.15. Pressure drop values for increasing distance between heat sources (Source: Vadakkan et al., 2004)

On the other hand, Aghvami and Faghri (2011) performed an analytical solution for two-dimensional thermo-fluid model of a flat heat pipe with different heating and cooling configurations as shown in Figure 1.16. Capillary pressure values and dry-out limitations were also determined in the study. The results showed that higher heat input through the evaporator causes maximum surface temperature, pressure drop and fluid velocity to be increased due to the elevated mass flow rate at the vapor-wick interface. Additionally, as demonstrated in Figure 1.17, thermal performance of the heat pipe is badly influenced (i.e. increased end to end temperature difference) by the reduction of

evaporative area because of the sudden increase in the peak wall temperature; and lower effective capillary pressure is obtained with increased heat input to the heat pipe evaporator.

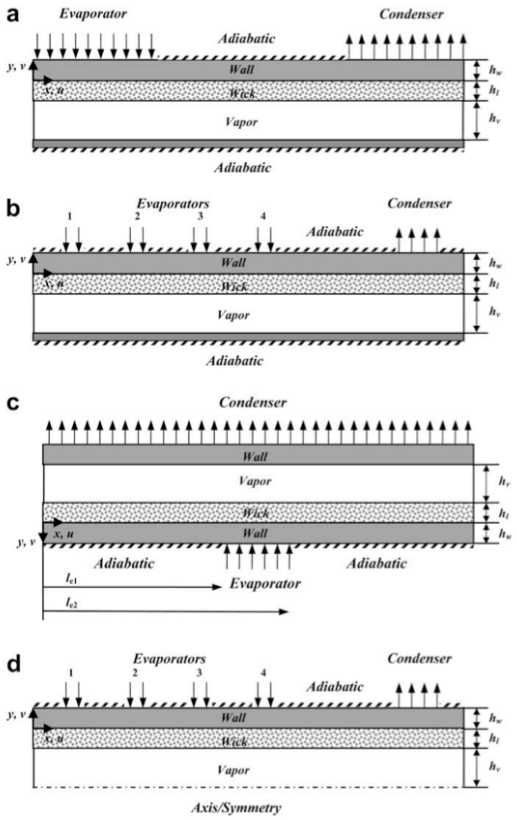


Figure 1.16. Flat heat pipe with a) single evaporator and condenser; b) multiple heat source and single condenser; c) evaporator at the bottom and condenser on the top; d) multiple heat source and single condenser with symmetry boundary condition (Source: Aghvami & Faghri, 2011)

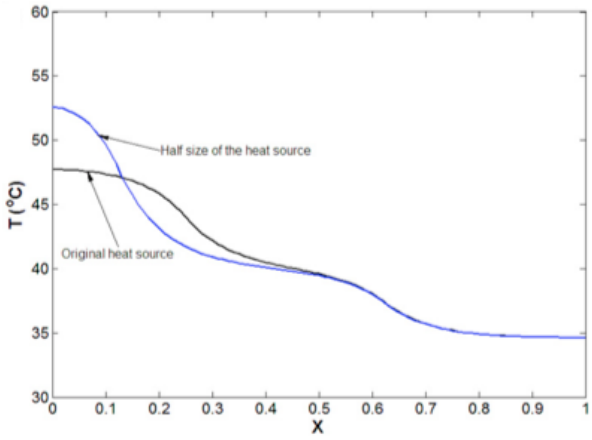


Figure 1.17. Axial wall temperature distribution for different heat source sizes (Source: Aghvami & Faghri, 2011)

The effect of gravity on the heat pipe performance was investigated by Hung and Tio (2012) for inclined micro heat pipes. A one dimensional steady state model was developed to see both favorable& adverse effects of gravity on thermal performance of heat pipe. Schematic diagram of positive and negative inclination is presented in Figure 1.18. Results indicated that negative inclination decreases rate of circulation of fluid and heat transport capacity of the heat pipe.

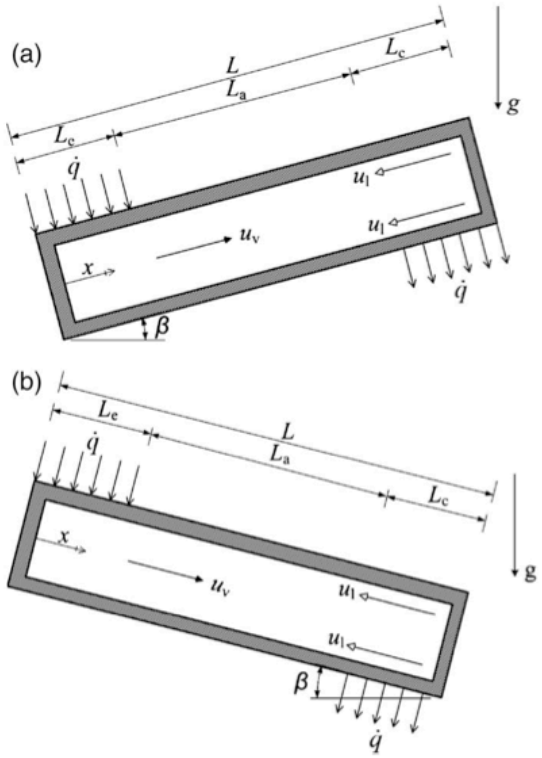


Figure 1.18. a) Positive inclination; b) Negative inclination
(Source: Hung & Tio, 2012)

Inversely, positive inclination enhances the rate of circulation and heat transport capacity. Normally, maximum liquid volume fraction occurs at the condenser end cap. However, in the case of positive inclination, liquid in the condenser is drawn towards the evaporator by means of gravitational force and maximum liquid volume fraction is shifted from condenser end cap to the condenser section itself. As a result, a throat within the condenser section is formed, which inhibits the vapor flow and this effect is undesirable in the heat pipe flow circulation.

Later on, Ranjan, Murthy, Garimella and Vadakkan (2010) performed a three dimensional numerical study in both macro and micro scale. Macro model was utilized to solve continuity, Navier-Stokes and energy equations while micro model considered

the effects of the meniscus curvature of the liquid in the wick structure, thin-film evaporation and Marangoni convection. A coupled solution of macro and micro models was proposed and it was concluded that coupled model results in a smaller thermal resistance compared to the original macro model. Furthermore, the difference between coupled and uncoupled model is small for low heat flux values and as the heat flux gets higher, the difference also tends to increase as be derived from Figure 1.19.

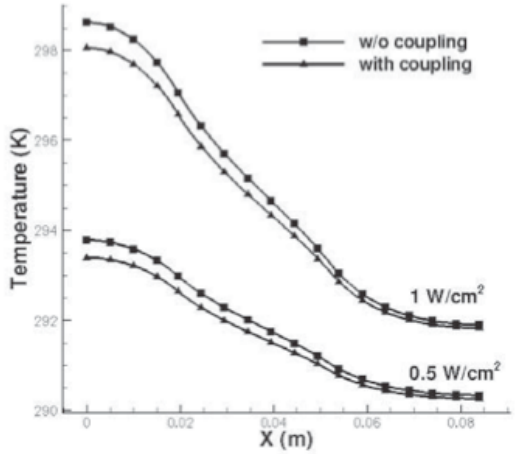


Figure 1.19. Temperature variation along x-direction for coupled and uncoupled models (Source: Ranjan et al., 2010)

In the present study, a steady state, two-dimensional, laminar and incompressible modeling is performed numerically to simulate a flat heat pipe with asymmetric boundary conditions. Finite volume method along with staggered grid arrangement and hybrid differencing scheme is applied to solve continuity, Navier-Stokes and energy equations. Brinkman-Forchheimer extended Darcy model is employed for the fluid flow in the wick structure. A MATLAB code is developed to solve the governing equations by using SIMPLE algorithm to obtain the liquid/vapor velocities, capillary pressure and pressure distribution within the heat pipe. The model accounts for uniform injection and suction in the evaporator and condenser sections and it is assumed that evaporation and condensation only occur in evaporator and condenser sections, respectively. Wick structure is presumed to be isotropic and saturated with working fluid. The interfacial velocity is found from energy balance at the liquid-vapor interface. The effects of evaporative heat flux and heat pipe aspect ratio are examined on the required capillary pressure and thermal performance of the heat pipe.

# CHAPTER 2

# MATHEMATICAL MODEL

In the present study, a flat heat pipe is modeled numerically in two-dimensional space. Vapor and wick regions are incorporated in the analysis; and continuity, momentum and energy equations are solved for steady state, subsonic, laminar, incompressible and Newtonian flow assumptions. Furthermore, thermo physical properties are taken as constant and no body forces are included in the model.

A schematic diagram of the flat heat pipe including the physical dimensions of each region is presented in Figure 2.1. As shown in the figure, the heat pipe under investigation consists of single evaporator and condenser with an adiabatic region connecting those two sections. Wick exists only on one side of the heat pipe and it is presumed to be fully saturated with working fluid. The heat inflow and outflow occur through this side. Upper side of the heat pipe is subjected to adiabatic region only. Therefore, the domain has asymmetric boundary conditions.

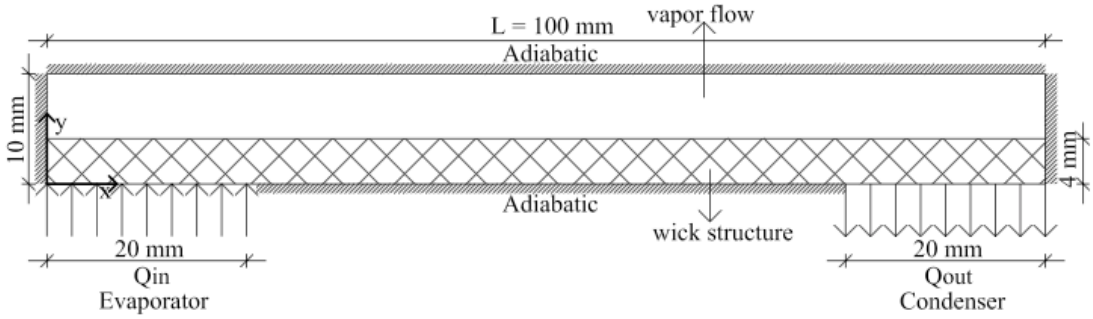


Figure 2.1. Schematic diagram of the domain with physical dimensions

Moreover, water and copper is used as working fluid and wick material of the heat pipe, respectively. Thermo physical properties of water for vapor and liquid phases along with the copper properties are presented in Table 2.1 for 323K which is the assumed operating temperature of the flat heat pipe in this study. The heat inflow and outflow are assumed to be equal to each other and their values are taken as 1 W/cm$^2$.

Sintered copper wick is utilized to the heat pipe with a porosity (ε) value of 0.52 and permeability (K) value of $9x10^{-13}$ m$^2$. Effective thermal conductivity of the wick

structure is calculated by using equation (2.1). In addition, Brinkman- Forchheimer extended Darcy model is applied to analyze the flow in the wick structure with Ergun coefficient's ($C_E$) being 0.55. (Ranjan et al., 2010)

$$k_{eff} = k_s \left( \frac{2 + k_l / k_s - 2\varepsilon(1 - k_l / k_s)}{2 + k_l / k_s + \varepsilon(1 - k_l / k_s)} \right) \tag{2.1}$$

Table 2.1. Thermo physical properties of heat pipe working fluid&wick material

| | | |
|---|---|---|
| **Copper** | Thermal conductivity (W/m.K) | 398 |
| **Liquid (Water)** | Density (kg/m$^3$) | 998.16 |
| | Dynamic viscosity (Pa.s) | 5571.10$^{-7}$ |
| | Thermal conductivity (W/m.K) | 0.6415 |
| | Specific heat (kJ/kg.K) | 4.182 |
| **Vapor (Water)** | Density (kg/m$^3$) | 0.09065 |
| | Dynamic viscosity (Pa.s) | 100.10$^{-7}$ |
| | Thermal conductivity (W/m.K) | 0.0208 |
| | Specific heat (kJ/kg.K) | 1.909 |
| **Water** | Latent heat of evaporation (kJ/kg) | 2382.7 |
| - | Gas constant (kJ/kg.K) | 0.461 |

Under the assumptions mentioned above, the governing equations (i.e. continuity, momentum and energy equations) for the wick and vapor region may be written in form shown below. The continuity equation, which is derived based on the conservation of mass, is presented below for the vapor and wick region:

$$\frac{\partial u}{\partial x} + \frac{\partial v}{\partial y} = 0 \tag{2.2}$$

However, momentum equations differ from each other for vapor and wick regions. Momentum equations are obtained by following Newton's second law of motion and they can also be called as Navier-Stokes equations for an incompressible Newtonian fluid. Two-dimensional Navier-Stokes equations for vapor flow are:

$$\rho_v u \frac{\partial u}{\partial x} + \rho_v v \frac{\partial u}{\partial y} = -\frac{\partial p}{\partial x} + \mu_v \left[ \frac{\partial^2 u}{\partial x^2} + \frac{\partial^2 u}{\partial y^2} \right] \tag{2.3}$$

$$\rho_v u \frac{\partial v}{\partial x} + \rho_v v \frac{\partial v}{\partial y} = -\frac{\partial p}{\partial y} + \mu_v \left[ \frac{\partial^2 v}{\partial x^2} + \frac{\partial^2 v}{\partial y^2} \right] \tag{2.4}$$

As discussed above, Brinkman- Forchheimer extended Darcy model is assumed for the liquid flow in the wick region. The porous wick is assumed to be isotropic and homogenous. Moreover, wick's solid structure and working fluid inside the wick are accepted to be in local thermal equilibrium. With all these considered, the momentum equations for the porous wick may be presented as:

$$\rho_l u\frac{\partial u}{\partial x}+\rho_l v\frac{\partial u}{\partial y}=-\varepsilon\frac{\partial p}{\partial x}+\mu_l\left[\frac{\partial^2 u}{\partial x^2}+\frac{\partial^2 u}{\partial y^2}\right]-\frac{\mu_l\varepsilon}{K}u-\frac{C_E\varepsilon}{K^{1/2}}\rho_l|u|u \tag{2.5}$$

$$\rho_l u\frac{\partial v}{\partial x}+\rho_l v\frac{\partial v}{\partial y}=-\varepsilon\frac{\partial p}{\partial y}+\mu_l\left[\frac{\partial^2 v}{\partial x^2}+\frac{\partial^2 v}{\partial y^2}\right]-\frac{\mu_l\varepsilon}{K}v-\frac{C_E\varepsilon}{K^{1/2}}\rho_l|v|v \tag{2.6}$$

Energy equation is derived by applying conservation of energy to the control volume. The energy equation for both vapor flow and the liquid flow within the heat pipe is the same except the conductivity values. Thermal conductivity of water vapor is used in the energy equation of the vapor flow while the conductivity value in the energy equation of the liquid flow is the effective thermal conductivity value that is found by using equation (2.1), shown above.

$$u\frac{\partial T}{\partial x}+v\frac{\partial T}{\partial y}=\frac{k_v}{\rho_v.c_{p,v}}\left[\frac{\partial^2 T}{\partial x^2}+\frac{\partial^2 T}{\partial y^2}\right] \tag{2.7}$$

$$u\frac{\partial T}{\partial x}+v\frac{\partial T}{\partial y}=\frac{k_{eff}}{\rho_l.c_{p,l}}\left[\frac{\partial^2 T}{\partial x^2}+\frac{\partial^2 T}{\partial y^2}\right] \tag{2.8}$$

These equations are non-linear set of equations, which are coupled to each other meaning that results from one of these equations cannot be obtained without solving the other equations. Therefore, they have to be treated together as a couple and solved simultaneously. Besides, there is no equation for the pressure values, which makes the solution even harder. Analytical solution methods for the above governing equations are extremely complicated and are not easy to solve without utilizing many assumptions and simplifications. Considering all of these difficulties, numerical methods are implemented to this set of equations to obtain solutions that are more reliable. Results can be obtained more efficiently by means of utilizing either commercial codes or in-house codes.

In the scope of this study, an in-house code is developed by using the software, MATLAB (The MatWorks, Inc.). The reason why the commercial codes are not preferred in this study is that they do not always offer too much flexibility to the users through the solution process of the equations. On the other hand, the parameters are totally controlled by the user himself in the case of in-house code development. In addition, as the flow and geometry of the domain become more complicated, use of commercial codes are inevitable and therefore, solutions by commercial codes must be validated thoroughly. In the manner of computational time, commercial codes may need weeks to solve a problem since they are designed to model any kind of flow. However, in-house codes are developed for special cases and optimizing the code for each case can reduce the solution time. Of course, knowing the problem that is dealt with is a great advantage in such a situation.

# CHAPTER 3

# NUMERICAL METHOD

Numerical modeling has become a widely used tool in most of the engineering applications. A physical phenomenon is transformed into a mathematical model, which is generally in the form of non-linear partial differential equation (PDE). Either analytical or numerical solution methods can be implemented to solve these non-linear PDEs. However, it is almost impossible to solve a non-linear PDE by utilizing only analytical methods without any assumptions and simplifications. Advanced mathematical skills are needed for the analytical solution methods even in the simplified forms. Thus analytical methods are very time-consuming. In such cases, numerical methods are usually preferred. What numerical methods focus on, is not the differential equation itself, but the linear algebraic equation that is obtained by employing discretization to the non-linear PDEs. Hence, numerical methods are composed of several steps that eventually lead to the solution of a physical problem. In this chapter, these steps shall be discussed.

## 3.1. General Transport Equation

The general transport equation in the differential form is presented below in Equation 3.1 for the steady case. In this equation, a general variable $\phi$ is introduced to be replaced with an either vectorial or scalar quantity depending on the equation needed. For instance, if velocity is substituted with $\phi$, momentum equations are obtained or if temperature is placed in the equation instead of $\phi$, energy equation is achieved. For $\phi$=1, the below equation turns into the continuity equation.

$$div\left(\rho\vec{V}\Phi\right) = div(\Gamma grad\Phi) + S_{\Phi} \tag{3.1}$$

Left hand side of the equation represents the convective terms while the right hands side includes diffusive and source terms, respectively. In other words, the above equation means that the net rate of flow of $\Phi$ due to convection equals to sum of the rate

of increase of Φ due to diffusion and rate of increase of Φ due to sources. Diffusion term, Γ, and source term, $S_{\Phi,}$ involve different parameters depending on the equation and the problem under investigation.

In order to solve above differential equation and find the dependent variable, Φ, the equation (3.1) should be discretized and given the form of linear algebraic equation. Discretization is performed by dividing the domain into smaller pieces and treating each piece separately. The division of the domain can be made by using different discretization techniques for partial differential equations. Finite element, finite difference and finite volume methods are the mostly utilized approaches and finite volume method (FVM), which is employed in the scope of this study, shall be explained in the next section.

## 3.2. Finite Volume Method (FVM)

As the first step of solving a differential equation, discretization is to be employed to the equation before performing any numerical evaluation. In order to discretize a non-linear partial differential equation by using FVM, the domain should initially be divided into a number of discrete volumes depending on the expected accuracy from the results. The division of the domain is also referred as grid generation and the resulting geometry can be called as meshed geometry. The equations will be solved at each discrete volume on the meshed geometry. FVM is applicable to any kind of geometries using different type of meshes. The main advantage of finite volume method is that fluxes are conserved locally from one each control volume to its neighbors and global maintenance of conservation is sustained throughout the domain automatically.

Below in Figure 3.1, a schematic view of a general nodal point identified by P is demonstrated with its neighbors. The positive directions of the coordinate axes are also indicated in the figure. Corresponding to its direction with regard to nodal point P (i.e. W symbolizes west direction), each capital letter represents the center of a neighbor cell. Small letters, on the other hand, symbolizes the cell surfaces that intersect with the neighbor cells.

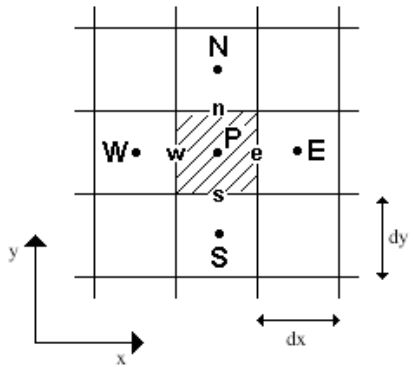


Figure 3.1. A schematic representation of a control volume

Volume integral formulation of the fluxes for each cell is then formed by considering the above control volume and its neighbors. Starting with equation (3.1), computational steps of the finite volume method is carried out. The resulting integration of the governing equations corresponding to each cell can be seen in the compact form in equation (3.2).

$$\int_{C.V.} div(\rho\vec{V}\Phi)dV = \int_{C.V.} div\left(\Gamma grad\Phi\right)dV + \int_{C.V.} S_{\Phi}\, dV \qquad (3.2)$$

The volume integral on the left hand side which, is the convective flux through the control volume and the first volume integral on the right hand side, which is the diffusion flux are to be rewritten in the form of surface integral by utilizing Gauss's divergence theorem. The theorem can be mathematically shown in equation (3.3) for any vector, V.

$$\int_{C.V.} div(\vec{V})dV = \int_{A} \vec{n}.\vec{V}dA \qquad (3.3)$$

On the right hand side of the equation (3.3), the vector n symbolizes the normal direction to the surface element *dA*. Thus, the dot product of vector "V" and vector "n" means the component of vector "V" in the direction of vector "n". According to the Gauss's divergence theorem shown above, the volume integral of the divergence of a vector "V" equals to the area integral of the component of vector "V" in the normal direction to surface. If Gauss's divergence theorem is applied to equation (3.2), then the equation (3.4) is obtained as can be seen below.

$$\int_A \vec{n}.(\rho\vec{V}\Phi)dA = \int_A \vec{n}.(\Gamma grad\Phi)dA + \int_{C.V.} S_\Phi\, dV \tag{3.4}$$

Equation (3.4) is the steady state convection-diffusion equation for general property Φ. The left hand side of above equation physically states the net rate of change of convection flux through control volume, in the direction of n, which is normal to the surface area. Furthermore, the first term on the right hand side of equation (3.4) is the mathematically written form of the net rate of change of diffusion flux through control volume in the normal direction to the surface. The last term on right hand side is the generation or destruction of dependent variable (Φ) within the control volume.

The integral formulation of the governing equations in compact form is obtained in equation (3.2). After applying Gauss's divergence theorem to this equation, the next step is to perform the integration of the governing equations for the control volume that is illustrated in Figure 3.1.

$$\begin{aligned}&(\rho u\Phi A)_e - (\rho u\Phi A)_w + (\rho v\Phi A)_n - (\rho v\Phi A)_s \\ &= \left(\Gamma A\frac{d\Phi}{dx}\right)_e - \left(\Gamma A\frac{d\Phi}{dx}\right)_w + \left(\Gamma A\frac{d\Phi}{dy}\right)_n - \left(\Gamma A\frac{d\Phi}{dy}\right)_s + \bar{S}\Delta V\end{aligned} \tag{3.5}$$

Equation (3.5) is the balance equation of inflow and outflow fluxes through the cell faces of the control volume in Figure 3.1. In the above equation, $A$ is the cross section, $\Delta V$ is the volume and $\bar{S}$ is the average value of the source term within the control volume. Moreover, Γ symbolizes the constant properties and may include different parameters depending on the equation under concern. The gradients on the right hand side of the equations and the velocity values at the cell faces, which are included in the convection terms, should be determined.

However, convective terms create serious problems during this process while the diffusion terms are very easy to be resolved. The reason why is that, the diffusion effects the dependent variable (Φ) in all directions in the domain regardless of the flow direction but convective terms influence the dependent variable in the flow direction so they have to be treated accordingly.

A quick and simple way of expressing the gradients in the diffusion terms and cell face velocity values in the convection terms may be introduced at this point, which is called central differencing. In central differencing, the variables are linearly

interpolated by using the values of the nodal points of the neighboring cells and reasonable results can still be proposed. However, different type of schemes, other than central differencing scheme, may also be employed to equation (3.5) depending on the relative strength of convective and diffusion terms. Before getting into the different type of schemes, new variables, F and D, are introduced to for the sake of simplicity of the equations.

Table 3.1. Expressions for the values of F and D

| **Cell Face** | **West** | **East** | **South** | **North** |
|---|---|---|---|---|
| **F** | $(\rho u A)_w$ | $(\rho u A)_e$ | $(\rho v A)_s$ | $(\rho v A)_n$ |
| **D** | $\left(\frac{\Gamma}{\delta x}A\right)_w$ | $\left(\frac{\Gamma}{\delta x}A\right)_e$ | $\left(\frac{\Gamma}{\delta y}A\right)_s$ | $\left(\frac{\Gamma}{\delta y}A\right)_n$ |

First, the F and D values in Table 3.1 are to be calculated on the cell face of the control volume by making use of the neighboring nodal points. Secondly, the coefficients of the nodal points, which are the combination of F and D values, are then obtained by means of different schemes. The most common schemes for the finite volume method are namely central differencing, upwind differencing, hybrid differencing and power law schemes and they are presented in Table 3.2.

Table 3.2. Neighbor coefficient values for different type of schemes
(Source: Versteeg & Malalasekera, 2007)

| **Scheme Type** | $a_W, a_S$ | $a_E, a_N$ |
|---|---|---|
| **Central Differencing** | $D_i + F_i/2$ | $D_j - F_j/2$ |
| **Upwind Differencing** | $D_i + \max(F_i, 0)$ | $D_j + \max(0, -F_j)$ |
| **Hybrid Differencing** | $\max\left[F_i, (D_i - F_i/2), 0\right]$ | $\max\left[-F_j, (D_j - F_j/2), 0\right]$ |
| **Power Law** | $D_i \max\left[0, (1-0.1\lvert Pe_i\rvert)^5\right]$ $+\max(F_i, 0)$ | $D_j \max\left[0, (1-0.1\lvert Pe_j\rvert)^5\right]$ $+\max(-F_j, 0)$ |

In the above table, the coefficients of the neighboring cells (i.e. $a_W$, $a_S$, $a_E$, $a_N$) for various schemes are evaluated by means of the values at the cell faces. The subscript "i" stands for west and south faces while subscript "j" represents the east and north

faces. The aim of all these operations is to obtain a nodal equation, which is composed of the values only at the cell centers since the values at the cell faces are unknown.

In addition, the properties such as the density (ρ), Γ, which may take different values depending on the equation type, and area (A), which is equal for each cell and each direction, are assumed to be constant in the scope of this study and can be taken out of the parentheses directly without utilizing any operation. With all these considered, the general form of the nodal equation is obtained in the form below.

$$a_P\Phi_P = a_E\Phi_E + a_W\Phi_W + a_N\Phi_N + a_S\Phi_S + b \tag{3.6}$$

Equation 3.6 represents the governing equations in two-dimensional space where subscript P indicates the nodal point of the cell whose values are to be evaluated. The rest of the subscripts indicate the neighboring cell coefficients and nodal points in the manner of direction according to the central nodal point. As can be seen, equation (3.6) is an algebraic equation and solving this kind of equations is relatively easier than solving an integral equation. The last term of equation (3.6) is the source term and it may be a function of the transported property Φ. Thus, it can be decomposed as:

$$b = S_u + S_P\Phi_P \tag{3.7}$$

However, choosing the appropriate scheme is another issue in the finite volume method. In order for a scheme to give reasonable outcome, the physical characteristics of the flow should be determined. The relative strength of convection terms and diffusion terms to each other, gives a clue for selection of the right scheme. At this point, it is necessary to introduce Peclet number (Pe). It is a dimensionless number, which is the ratio of the convective transport rate to the diffusive transport rate.

$$Pe = \frac{F}{D} \tag{3.8}$$

Equation (3.8) represents the mathematical formulation of the Peclet number. Before choosing the scheme type, which will be incorporated to the integrated equation, the Peclet number is calculated. By this means, the degree of how much the transported

property is affected by the flow direction is determined and scheme type is selected accordingly.

In fact, central differencing scheme, which is considered to be second order accurate for |Pe|<2, can be employed to many flow simulations but in the situations where the direction of flow has a serious effect on the distribution of the dependent variable, the control volume should be very small, which means the number of the computational cells should be infinitely large. Otherwise dependable results cannot be obtained. But a finite number of cells is desired for flow simulations. In such cases, the calculations take relatively very long time. Thus, the schemes should be chosen very carefully and some certain fundamental properties should be concerned to yield the most reliable results with the lowest possible run time.

Upwind scheme proposes an improvement to the central differencing scheme, which does not possess the ability to include the flow direction into the calculations. In other words, the control volume is not affected in the same amount by its neighboring cells if a highly convective flow is under concern and this fact influences the results. In Table 3.2, the forms of the coefficients are presented in the case of utilizing upwind differencing scheme. Upwind scheme is often the best scheme to initiate the calculations with. Accuracy of this scheme is in the first order.

In addition, the velocity throughout the domain may not be constant in many cases. Therefore, it is possible that some sections of the domain are highly affected by the flow direction while some sections are not. A combination of central differencing scheme and upwind scheme may offer the most accurate results to the exact solution. This scheme is called the hybrid scheme. In hybrid differencing scheme, for Pe<2, central differencing scheme is utilized and for |Pe|>2, upwind scheme is used and diffusion is set to zero. A form of notation for hybrid scheme is tabulated in Table 3.2.

On the other hand, Figure 3.2 shows the dependent variable values computed with various schemes for a range of Peclet number from -10 to 10. The figure also proves that it does not seem logical to set the diffusion effects equal to zero as soon as |Pe|>2 since diffusion still have an impact on the dependent variable distribution. That is why another approximation called the power law scheme is proposed for the coefficients of the discretized equation. Power law scheme is very similar to hybrid scheme, except that power law produces better results than the hybrid scheme for varying Peclet numbers. In power law scheme, the diffusion effects are set to zero when |Pe| exceeds 10. If |Pe| stays in the region between 0 and 10, the coefficients are

represented by a polynomial expression as shown in Table 3.2. Otherwise, the diffusion is ignored and upwind scheme is used. The only disadvantage of the power law scheme is that it is considered to be first order accurate.

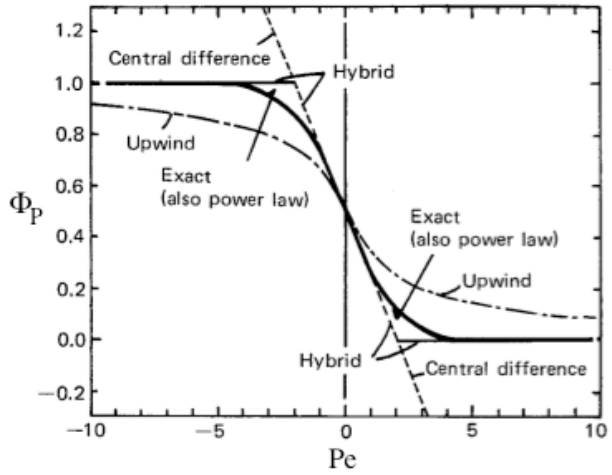


Figure 3.2. Calculated values of $\Phi_P$ with different scheme types for a range of Pe (Source: Suhas V. Patankar, 1980)

In the current study, the Peclet number stays in the range of -2 and 2. Therefore, hybrid-differencing scheme is employed for the discretization. After calculating the coefficients of the neighboring cells with the help of Table 3.2, next thing to evaluate is the central coefficient of the transported property Φ. For the hybrid scheme, the central coefficient can be calculated as shown in Equation 3.9.

$$a_P = a_W + a_E + a_S + a_N + (F_e - F_w) + (F_n - F_s) - S_P \qquad (3.9)$$

In the above equation, $S_P$, which is also shown in equation (3.7), includes the effects of source terms to the central node and its value changes depending on the boundary conditions, which shall be investigated in Chapter 5. Here, one fact should be emphasized, though. By adding $S_P$ to the central coefficient $a_P$, the source term b in equation (3.6) changes and it involves only $S_u$, which is a term independent from the transported property.

Up until now, the pressure gradients in the momentum equations were excluded while explaining the discretization process and the real problem begins with the inclusion of the pressure term to the nodal equations. In some references, the pressure term is represented as a part of the source term. However, it is investigated separately in

the current study. Therefore, the discretized momentum equation, with $S_\Phi$ integrated into $a_P$, becomes as follows:

$$a_P\Phi_P = a_E\Phi_E + a_W\Phi_W + a_N\Phi_N + a_S\Phi_S + A.\Delta P + S_u \qquad (3.10)$$

ΔP in equation (3.10) is the pressure difference between the nodal points of the control volume and its neighbors. A is the area and its value may vary according to the grid dimensions throughout the domain.

On the other hand, energy equation does not contain any pressure term so no extra attention is needed to solve energy equation. The equations, which involve velocity and pressure terms at the time, are called pressured linked equations and some algorithms have been developed for the pressure- velocity coupling in them. These algorithms make use of different kinds of grid arrangements to overcome the problems created by the pressure terms. Thus, an intimate attention should be given to the grid arrangement. In the next chapter, the selected grid arrangement type and the solution algorithm to solve the distribution of the transported property Φ shall be presented.

# CHAPTER 4

# SOLUTION ALGORITHM

## 4.1. Introduction

Modeling of the heat and fluid flow inside heat pipe basically means the evaluation of the velocity, pressure and temperature distributions of vapor and liquid flow within the heat pipe. In order to calculate all these distributions continuity, momentum and energy equations are to be solved mathematically and the results of these equations are utilized to make a physical sense to the real operations occurring in the heat pipe. The continuity, momentum and energy equations in two-dimensional coordinate system are presented below for incompressible vapor flow in a flat heat pipe.

$$\frac{\partial}{\partial x}(\rho u)+\frac{\partial}{\partial y}(\rho v)=0 \tag{4.1}$$

$$\frac{\partial}{\partial x}(\rho_v uu)+\frac{\partial}{\partial y}(\rho_v vu)=-\frac{\partial p}{\partial x}+\frac{\partial}{\partial x}\left(\mu_v\frac{\partial u}{\partial x}\right)+\frac{\partial}{\partial y}\left(\mu_v\frac{\partial u}{\partial y}\right)+S_u \tag{4.2}$$

$$\frac{\partial}{\partial x}(\rho_v uv)+\frac{\partial}{\partial y}(\rho_v vv)=-\frac{\partial p}{\partial y}+\frac{\partial}{\partial x}\left(\mu_v\frac{\partial v}{\partial x}\right)+\frac{\partial}{\partial y}\left(\mu_v\frac{\partial v}{\partial y}\right)+S_v \tag{4.3}$$

$$\frac{\partial}{\partial x}(\rho_v uT)+\frac{\partial}{\partial y}(\rho_v vT)=\frac{\partial}{\partial x}\left(\frac{k_v}{c_{P,v}}\frac{\partial T}{\partial x}\right)+\frac{\partial}{\partial y}\left(\frac{k_v}{c_{P,v}}\frac{\partial T}{\partial y}\right)+S_T \tag{4.4}$$

The equations (4.1)-(4.4) contain velocity, pressure and temperature gradients. In general, the velocity field in the domain is unknown. So are pressure and temperature fields. Thus, these equations are coupled to each other in nature and should be solved simultaneously, which complicates the solution. Besides, there are some non-linear terms that make the solution even harder.

Even though, the u and v velocities appear in all of the above equations, pressure exists only in the momentum equations. In addition, the velocity values should satisfy

the Equation 4.1, which is the continuity equation but there is no separate equation for the pressure. All in all, there are four equations with none of their parameters known. In such a case, if the pressure distribution in the flow is known beforehand, the rest of the equations can be solved by using the schemes, which are presented in the previous chapter. If the flow is compressible, pressure can be found by employing the equation of state in which P is a function of density and temperature. The compressibility of the flow results in a change in the density so the pressure gradient can be obtained. Once the pressure gradient is determined, the correct velocity distributions, which also satisfy the continuity equation, are obtained. However, since the flow is assumed to be incompressible (i.e. density is constant) in the scope of this study, it is impossible to utilize the equation of state.

The problems arising from both pressure gradient and non-linearity can be overcome by using iterative methods. One of these methods called SIMPLE algorithm was first proposed by S. V. Patankar and Spalding (1972). SIMPLE stands for "Semi-Implicit Method for Pressure Linked Equations". It is an extensively used numerical procedure to solve Navier-Stokes equations (momentum equations for Newtonian fluid flow) in CFD problems. In SIMPLE algorithm, guessed velocity and pressure fields are formed. To correct the guessed pressure field, a pressure correction equation is then obtained by using continuity equation. After correcting the pressure field, the velocity fields are also updated and this process continues until the convergence criteria, which are defined by the user, are satisfied.

However, special treatment to the grid generation should still be given even if SIMPLE algorithm is integrated into the solution. One of the easy ways to constitute the grid arrangement is to assign both scalar and vectorial variables to the center of the node. This type of grid is called the collocated grid. The implementation of collocated grid arrangement is very easy even for the complex geometries and it diminishes the complexity of the algorithm and reduces the computational time. The disadvantage of utilizing the collocated grid arrangement is that it may create interpolation errors when the distribution of the transported property is very wavy. Hence, staggered grid arrangement is offered to avoid the interpolation errors.

## 4.2. Staggered Grid

As mentioned earlier, staggered grid arrangement is utilized when the inspected domain has an extremely wavy regime. Staggered grid suggests that the values at the cell center should be used for scalar variables such as temperature and pressure while the values at the cell faces are taken for the vectorial variables such as velocity. Hence, the velocity control volumes in both directions are shifted backwards in order to intersect the center of vectorial nodes with the cell face of the scalar nodes. Figure 4.1 visualizes the staggered grid arrangement. The intersections of the solid lines are the points where scalar variables are stored. The scalar control volumes are also called as the pressure control volumes since the pressure correction equation is formed by employing continuity equation within this control volume. On the other hand, the horizontal arrows indicate the locations where the u-velocity values are stored while the vertical arrows mark the center of v-velocity cells.

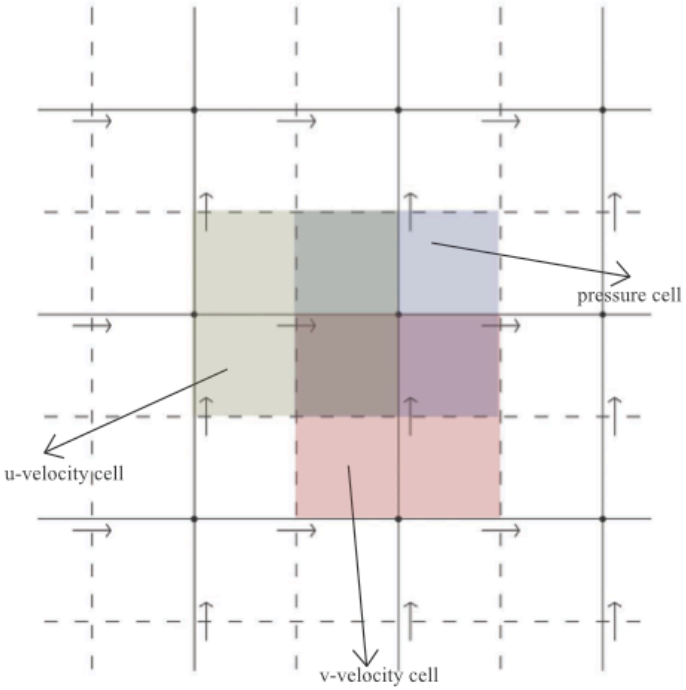


Figure 4.1. Schematic view of staggered grid

In Figure 4.1, it can be clearly seen that the cell faces (i.e. dashed lines) of the pressure nodes coincide with the center of the velocity nodes. This kind of arrangement avoids the unrealistic results due to the fluctuations of transported property. Furthermore, since the velocity values at cell faces are required in the scalar variable

calculations, such as energy equation, interpolation of the velocities are not required so the energy equation causes no problems unlike momentum equations do.

However, staggered grid arrangement complicates the grid formulation because some extra nodes (i.e. velocity nodes) are formed whose centers are indicated with arrows in Figure 4.1. Hence, the dashed lines require another notation system compatible with the existing notation system, which is used for the solid lines. In order to distinguish the cell centers from cell faces in the equations, the cell centers are symbolized with capital letters (i.e. I, J) while the cell faces are identified with small case letters (i.e. i, j) as illustrated in Figure 4.2. These notations are in the x and y directions, respectively.

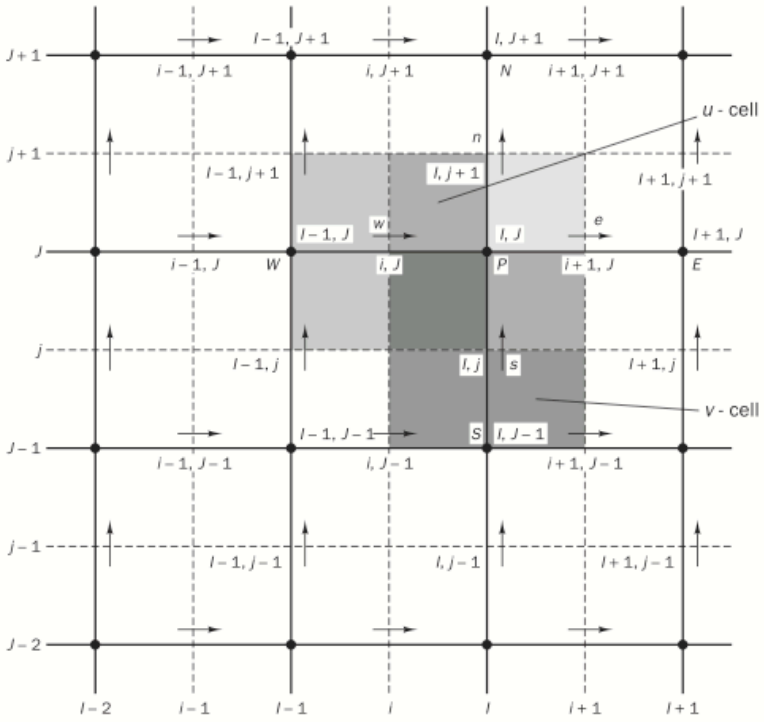


Figure 4.2. Schematic view of staggered grid with notations
(Source: Versteeg & Malalasekera, 2007)

Consequently, the point "P", which is the center of the pressure node, is presented with "I, J" in this notation system while u-velocity and v-velocity vectors are donated with "i, J" and "I, j", respectively as can also be seen in the figure above. On the other hand, in the manner of directional coordinates, the cell centers are defined by capital letters such as W, E, N and S and small case letters such as w, e, n, and s constitute cell faces. For example, u velocity on the west side is at "i, J" and can be

identified as $u_{i,J}$ or $u_w$. This kind of system creates problems during code development since the domain includes two notation systems. Furthermore, it consumes relatively more memory for complicated domain dimensions. However, more realistic results are obtained by employing staggered grid to the investigated flow problem. Therefore, the discretized equations are constituted by means of staggered grid arrangement.

## 4.3. Momentum Equations

In this section, the discretized equations shall be presented with the notation system based on staggered grid. However, only the momentum equations of vapor flow are discretized here for the sake of clarity. For the liquid flow momentum equations, some additional terms should be inserted into the vapor flow equations. Staggered grid can be implemented by using either backward velocity grids or forward velocity grids. In this study, backward-staggered grid is selected.

A subscript system is utilized to show the cell centers and faces as explained above. A detailed grid visualization of the u-control volume is presented in Figure 4.3. Considering all these, the discretized u-momentum equation can be written as follows.

$$a_{i,J}u_{i,J} = a_{i-1,J}u_{i-1,J} + a_{i+1,J}u_{i,+1J} + a_{i,J-1}u_{i,J-1} + a_{i,J+1}u_{i,J+1} + (p_{I-1,J} - p_{I,J}).A_{i,J} + b_{i,J} \qquad (4.5)$$

In equation (4.5), the coefficients of u velocities at different cell faces are determined by using the hybrid-differencing scheme. According to this scheme, the coefficients can take different values depending on the Peclet number. Nevertheless, these coefficients are composed of F and D values where F is the convective flux per unit mass and D is the diffusive flux per unit mass, respectively. Applying the new notation system, the values of the F and D can be calculated by an averaging procedure as shown below.

$$F_w = (\rho_v uA)_w = \frac{1}{2}\rho_v A_{i,J}(u_{i,J} + u_{i-1,J}) \qquad (4.6)$$

$$F_e = (\rho_v uA)_e = \frac{1}{2}\rho_v A_{i,J}(u_{i,J} + u_{i+1,J}) \qquad (4.7)$$

$$F_s = (\rho_v v A)_s = \frac{1}{2}\rho_v A_{I,j}(v_{I,j} + v_{I-1,j}) \tag{4.8}$$

$$F_n = (\rho_v v A)_n = \frac{1}{2}\rho_v A_{I,j}(v_{I,j+1} + v_{I-1,j+1}) \tag{4.9}$$

$$D_w = \left(\frac{\Gamma}{\delta x}A\right)_w = \frac{\mu_v}{\Delta x}A_{i,J} \tag{4.10}$$

$$D_e = \left(\frac{\Gamma}{\delta x}A\right)_e = \frac{\mu_v}{\Delta x}A_{i,J} \tag{4.11}$$

$$D_s = \left(\frac{\Gamma}{\delta y}A\right)_s = \frac{\mu_v}{\Delta y}A_{I,j} \tag{4.12}$$

$$D_n = \left(\frac{\Gamma}{\delta y}A\right)_n = \frac{\mu_v}{\Delta y}A_{I,j} \tag{4.13}$$

One thing should be emphasized here that the physical properties such as density and viscosity are assumed to be constant throughout the domain so these properties are taken out of the parentheses without applying any interpolation through the equations (4.6)-(4.13) and the equations (4.15)-(4.22).

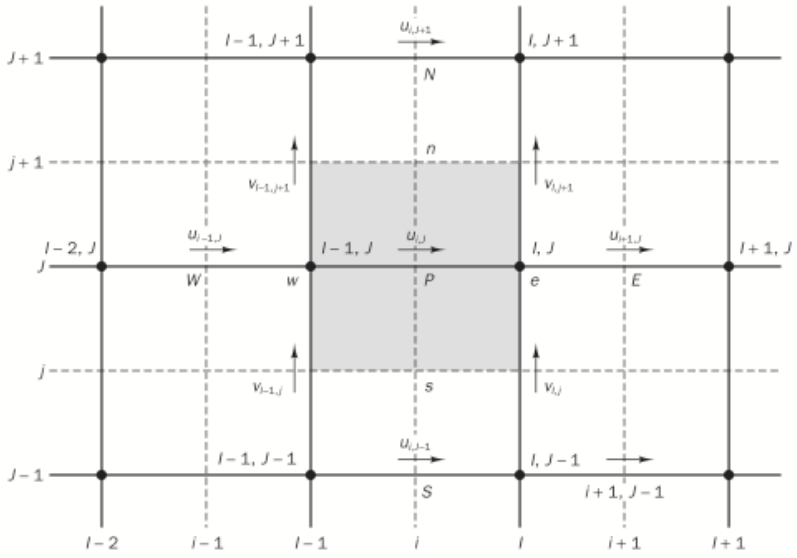


Figure 4.3. Visualization of u-control volume for backward-staggered grid (Source: Versteeg & Malalasekera, 2007)

Similarly, the momentum equation for the v-control volume is shown in equation (4.14). The v-velocity control volume and its neighboring v-velocity components are given in Figure 4.4 for better understanding of the discretized v-momentum equation.

$$a_{I,j}v_{I,j} = a_{I-1,j}v_{I-1,j} + a_{I+1,j}v_{I+1,j} + a_{I,j-1}v_{I,j-1} + a_{I,j+1}v_{I,j+1} + (p_{I,J-1} - p_{I,J}).A_{I,j} + b_{I,j} \quad (4.14)$$

It should be noted that point "P" in the center of the u-velocity and v-velocity control volumes should not be mixed with the pressure variable. Scalar variables such as pressure are located at the intersection of solid lines and "P" in Figure 4.3 and Figure 4.4 represent the cell centers of the velocity nodes.

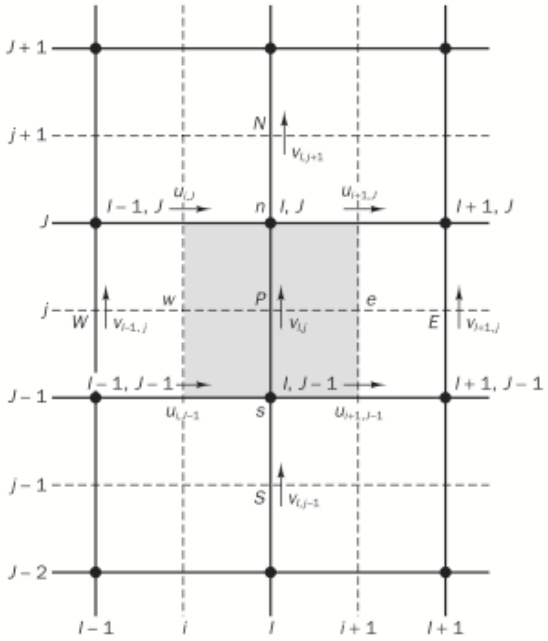


Figure 4.4. Visualization of v-control volume for backward-staggered grid (Source: Versteeg & Malalasekera, 2007)

The coefficients of the v-velocity values are again formed by utilizing the hybrid-differencing scheme. However, the convective flux values differentiate from the ones in u-velocity.

$$F_w = (\rho_v uA)_w = \frac{1}{2}\rho_v A_{i,J}(u_{i,J} + u_{i,J-1}) \quad (4.15)$$

$$F_e = (\rho_v u A)_e = \frac{1}{2}\rho_v A_{i,J}(u_{i+1,J} + u_{i+1,J-1}) \tag{4.16}$$

$$F_s = (\rho_v v A)_s = \frac{1}{2}\rho_v A_{I,j}(v_{I,j-1} + v_{I,j}) \tag{4.17}$$

$$F_n = (\rho_v v A)_n = \frac{1}{2}\rho_v A_{I,j}(v_{I,j} + v_{I,j+1}) \tag{4.18}$$

$$D_w = \left(\frac{\Gamma}{\delta x}A\right)_w = \frac{\mu_v}{\Delta x}A_{i,J} \tag{4.19}$$

$$D_e = \left(\frac{\Gamma}{\delta x}A\right)_e = \frac{\mu_v}{\Delta x}A_{i,J} \tag{4.20}$$

$$D_s = \left(\frac{\Gamma}{\delta y}A\right)_s = \frac{\mu_v}{\Delta y}A_{I,j} \tag{4.21}$$

$$D_n = \left(\frac{\Gamma}{\delta y}A\right)_n = \frac{\mu_v}{\Delta y}A_{I,j} \tag{4.22}$$

Remember that all of the above equations involve velocity values in both directions. However, the answers to these equations, themselves, give the velocity values. Hence, an iteration process is needed and each iteration in the loop uses the values of the previous iteration. This loop continues until the convergence criteria are satisfied.

In addition, the discretized equations can be used if and only if pressure distribution inside the domain is known. Indeed, in many cases pressure distribution is one of the unknowns. Considering this fact, an equation to calculate the pressure is required. At this point, the SIMPLE algorithm plays a very important role by turning the useless continuity equation into a very substantial equation.

## 4.4. The SIMPLE Algorithm

Semi-Implicit Method for Pressure-Linked Equations, also known as SIMPLE method, is a guess and correct iteration procedure. This method offers a way to make

use of continuity equation in order to solve all other discretized equations. First of all, the momentum equations are solved by using the guessed velocity components and guessed pressure field. Secondly, a pressure correction equation is formed by using the continuity equation. The guessed velocity and pressure fields are then corrected with the pressure correction equation and the loop is maintained until the desired convergence criteria are reached.

To avoid the confusion, the guessed values are written as p*, u* and v* while the correction values are symbolized as p', u' and v'. The algorithm is initiated by solving the equations (4.5) and (4.14) with the guessed velocity and pressure fields. For the sake of simplicity, all the neighboring terms are collected under a summation sign as follows.

$$a_{i,J}u^*_{i,J} = \sum a_{nb}u^*_{nb} + (p^*_{I-1,J} - p^*_{I,J}).A_{i,J} + b_{i,J} \tag{4.23}$$

$$a_{I,j}v^*_{I,j} = \sum a_{nb}v^*_{nb} + (p^*_{I,J-1} - p^*_{I,J}).A_{I,j} + b_{I,j} \tag{4.24}$$

After equations (4.23) and (4.24) are solved, p* is then corrected with the pressure correction value, p'.

$$p = p^* + p' \tag{4.25}$$

By analogy, the guessed velocity terms are also corrected with velocity corrections u' and v'.

$$u = u^* + u' \tag{4.26}$$

$$v = v^* + v' \tag{4.27}$$

At this point, equations (4.23) and (4.24) are subtracted from equations (4.5) and (4.14). Consequently, the below equations are obtained.

$$a_{i,J}(u_{i,J} - u^*_{i,J}) = \sum a_{nb}(u_{nb} - u^*_{nb}) + \left[(p_{I-1,J} - p^*_{I-1,J}) - (p_{I,J} - p^*_{I,J})\right].A_{i,J} \tag{4.28}$$

$$a_{I,j}(v_{I,j} - v^*_{I,j}) = \sum a_{nb}(v_{nb} - v^*_{nb}) + \left[(p_{I,J-1} - p^*_{I,J-1}) - (p_{I,J} - p^*_{I,J})\right].A_{I,j} \tag{4.29}$$

Substituting the equations (4.25)-(4.27) into equations (4.28) and (4.29), the resulting set of equations can be presented as:

$$a_{i,J}u'_{i,J} = \sum a_{nb}u'_{nb} + (p'_{I-1,J} - p'_{I,J}).A_{i,J} \tag{4.30}$$

$$a_{I,j}v'_{I,j} = \sum a_{nb}v'_{nb} + (p'_{I,J-1} - p'_{I,J}).A_{I,j} \tag{4.31}$$

In the equations (4.30) and (4.31), the neighboring terms (i.e. $a_{nb}u'_{nb}$ and $a_{nb}v'_{nb}$) are omitted as an approximation of SIMPLE algorithm. This simplification reduces the future complexities and the remaining terms are used as the velocity correction equations.

$$u'_{i,J} = d_{i,J}(p'_{I-1,J} - p'_{I,J}) \tag{4.32}$$

$$v'_{I,j} = d_{I,j}(p'_{I,J-1} - p'_{I,J}) \tag{4.33}$$

In equations (4.32) and (4.33), a new variable "d" is introduced, which can be defined as:

$$d_{i,J} = \frac{A_{i,J}}{a_{i,j}} \tag{4.34}$$

$$d_{I,j} = \frac{A_{I,j}}{a_{I,j}} \tag{4.35}$$

The equations (4.32) and (4.33) can be replaced with the velocity correction values in the equations (4.26) and (4.27) which gives:

$$u_{i,J} = u^*_{i,J} + d_{i,J}(p'_{I-1,J} - p'_{I,J}) \tag{4.36}$$

$$v_{I,j} = v^*_{I,j} + d_{I,j}(p'_{I,J-1} - p'_{I,J}) \tag{4.37}$$

The next thing to do in the SIMPLE algorithm is to make use of continuity equation to achieve pressure correction value. Keeping in mind that velocity values are

stored at the cell faces, a continuity equation can be written within a pressure control volume, whose center is on point (I, J), by using the velocity values on points (i, J), (i+1, J), (I, j) and (I, j+1). The velocity formula on points (i, J) and (I, j) are presented in equations (4.36) and (4.37), respectively. Similarly, the expressions for $u_{i+1,J}$ and $v_{i,J+1}$ can be found as:

$$u_{i+1,J} = u^{*}_{i+1,J} + d_{i+1,J}(p'_{I,J} - p'_{I+1,J}) \tag{4.38}$$

$$v_{I,j+1} = v^{*}_{I,j+1} + d_{I,j+1}(p'_{I,J} - p'_{I,J+1}) \tag{4.39}$$

$$where\ d_{i+1,J} = \frac{A_{i,J}}{a_{i,J}}\ and\ d_{i,J+1} = \frac{A_{i,J+1}}{a_{i,J+1}} \tag{4.40}$$

By discretizing the equation (4.1) according to the pressure control volume shown in Figure 4.4, the continuity equation can be expressed as follows:

$$\left[(\rho uA)_{i+1,J} - (\rho uA)_{i,J}\right] + \left[(\rho vA)_{I,j+1} - (\rho vA)_{I,j}\right] = 0 \tag{4.41}$$

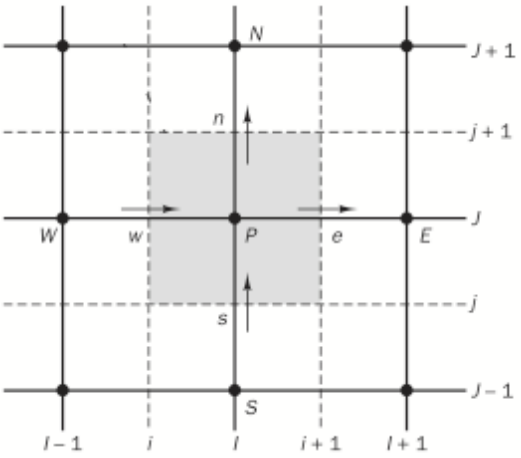


Figure 4.5. The pressure control volume
(Source: Versteeg & Malalasekera, 2007)

The velocity terms in equation (4.41) are found through equations (4.36)-(4.39) and those velocity expressions are replaced with the appropriate velocity values in equation (4.41). After some mathematical manipulations, the pressure correction equation is obtained in the form given below.

$$a_{I,J}p'_{I,J} = a_{I+1,J}p'_{I+1,J} + a_{I-1,J}p'_{I-1,J} + a_{I,J+1}p'_{I,J+1} + a_{I,J-1}p'_{I,J-1} + b'_{I,J} \qquad (4.42)$$

The coefficients and the source term of equation (4.42) are presented in the Table 4.1, which is shown below.

Table 4.1. The coefficients and the source term of pressure correction equation

| $a_{I+1,J}$ | $a_{I-1,J}$ | $a_{I,J+1}$ | $a_{I,J-1}$ | $b'_{I,J}$ |
|---|---|---|---|---|
| $(\rho dA)_{i+1,J}$ | $(\rho dA)_{i,J}$ | $(\rho dA)_{I,j+1}$ | $(\rho dA)_{I,j}$ | $(\rho u^* A)_{i,J} - (\rho u^* A)_{i+1,J} + (\rho v^* A)_{I,j} - (\rho v^* A)_{I,j+1}$ |

In addition, the coefficient $a_{I,J}$ can be expressed as:

$$a_{I,J} = a_{I+1,J} + a_{I-1,J} + a_{I,J+1} + a_{I,J-1} \qquad (4.43)$$

Equation (4.42) is employed to find the correction pressure field inside the domain and the guessed velocity and pressure fields are corrected with this equation. The last term in equation (4.42) represents the error caused by guessed velocity fields in every single iteration. When the convergence criteria are reached the pressure correction equation equals to zero and the iteration process stops. However, the promptness in satisfying the convergence may be manipulated by applying relaxation during the velocity and pressure correction step. Another advantage of relaxation is to prevent divergence of the solution. At this point, a relaxation factor "α" should be defined and relaxation can be performed as follows:

$$\Phi_{new} = (1-\alpha).\Phi_{old} + \alpha.\Phi_{calculated} \qquad (4.44)$$

In equation (4.44), if the value of α is selected as 1, the new transported variable is not affected by the previous iteration at all. On the other hand if it is chosen to be 0, the transported value is not corrected by the correction values and this has no meaning since guessed fields should be corrected somehow. That is why a value between 0 and 1 is determined for α to combine the effects of both the previous iteration and the correction process. In such a case, the relaxation process is called under-relaxation. In this study, various under-relaxation factors are tried and the relaxation factor are chosen to be 0.7 and 0.3 for velocity relaxations and pressure relaxation, respectively.

In order for SIMPLE algorithm to be understood in a more clear way, the whole operations carried out within the scope of this algorithm are summarized below in sequence.

1. The momentum equations are solved by using the guessed velocity and pressure fields.
2. Pressure correction equation is solved.
3. Pressure and velocity fields are corrected by using equations (4.25), (4.36) and (4.37).
4. All other discretized equations are solved.
5. The convergence criteria are checked. If they are satisfied, the algorithm is terminated.
6. If the convergence is not satisfied, new guessed values are assigned.

There are also some other algorithms to solve the momentum equations such as SIMPLER, SIMPLEC and PISO. SIMPLER algorithm is the improved version of SIMPLE and the pressure is corrected by a separate equation unlike SIMPLE method, which uses the same expression to correct the velocities and pressure. Thus, SIMPLER gives better pressure results compared to SIMPLE algorithm. However, SIMPLE method involves less calculation than SIMPLER. Furthermore, the effectiveness of the other algorithms is as good as SIMPLER for particular problems but they have not been examined thoroughly in the literature. That is why SIMPLE method is preferred over the other algorithms in this study.

## 4.5. Energy Equation

As mention in step 4, there may be some other equations to be solved to model a flow. In this study, temperature distribution inside the heat pipe is also investigated. In this regard, the energy equation is to be solved to find the temperature of each grid by using finite volume method and the distribution within the heat pipe is then determined. The energy equation in discretized form and its coefficients are presented below. The schematic view of the temperature control volume is the same as the pressure node

given in Figure 4.4. It should be noted that equation (4.45) is written only for vapor flow in the heat pipe.

$$a_{I,J}T_{I,J} = a_{I+1,J}T_{I+1,J} + a_{I-1,J}T_{I-1,J} + a_{I,J+1}T_{I,J+1} + a_{I,J-1}T_{I,J-1} \tag{4.45}$$

$$F_w = (\rho_v uA)_w = \rho_v A_{i,J} u_{i,J} \tag{4.46}$$

$$F_e = (\rho_v uA)_e = \rho_v A_{i,J} u_{i+1,J} \tag{4.47}$$

$$F_s = (\rho_v vA)_s = \rho_v A_{I,j} v_{I,j} \tag{4.48}$$

$$F_n = (\rho_v vA)_n = \rho_v A_{I,j} v_{I,j+1} \tag{4.49}$$

$$D_w = \left(\frac{\Gamma}{\delta x}A\right)_w = \frac{k}{c_p \Delta x}A_{i,J} \tag{4.50}$$

$$D_e = \left(\frac{\Gamma}{\delta x}A\right)_e = \frac{k}{c_p \Delta x}A_{i,J} \tag{4.51}$$

$$D_s = \left(\frac{\Gamma}{\delta y}A\right)_s = \frac{k}{c_p \Delta y}A_{I,j} \tag{4.52}$$

$$D_n = \left(\frac{\Gamma}{\delta y}A\right)_n = \frac{k}{c_p \Delta y}A_{I,j} \tag{4.53}$$

It can be seen in the above equations that, energy equation does not involve any pressure terms. Besides, the correct velocity fields are already found by solving momentum equations with the help of pressure correction equation. Thus, solving energy equation is a very straightforward process compared to momentum equations.

## 4.6. Convergence Criterion

For an iterative process to be successful, there are some certain conditions that needs to be satisfied. Since the iteration process is initiated by guessed velocity and pressure fields, the possibility of obtaining the correct fields right away is very low

unless by chance. That is why, some convergence criteria should be determined beforehand in order to have reliable results without performing unnecessary work. There are various methods to utilize the proper convergence. One of these ways is to monitor the difference of the results obtained by two successful iteration processes. However, this may not be a wise convergence criterion depending on the flow under investigation. Therefore, the residuals of the continuity, momentum and energy equations are monitored in the scope of this study. The general form of residual expression for momentum and energy equations as well as the pressure residual expression are given below. It should be emphasized that the pressure gradient term is now included into the source term for the sake of simple appearance.

$$R_{\Phi} = \frac{\left(b_{\Phi} + \sum a_{nb}\Phi_{nb}\right)}{a_P} - \Phi_P \tag{4.54}$$

$$R_P = \rho_v A_{i,J}(u_{i-1,J} - u_{i,J}) + \rho_v A_{I,j}(v_{I,j} - v_{I,j+1}) \tag{4.55}$$

Note that; there is no source term for temperature residual so $b_{\Phi}$ in equation (4.54) is excluded while the residual for energy equation is calculated. In addition, equation (4.55) is the mass imbalance of the control volume and it should be equal to zero so are the residual values of velocity and temperature. Hence, the smaller the residuals are, the more accurate the answers are. The iteration process stops if mass residual reaches $10^{-9}$.

# CHAPTER 5

# BOUNDARY CONDITIONS AND THEIR IMPLEMENTION

The boundary conditions are of high importance in numerical modeling since the correct fields are computed by means of boundary conditions which represent the interactions of the domain with its surrounding. Various boundary conditions may result in quite different simulation results. That is why boundary condition should be properly handled and implemented to the numerical model carefully to avoid any non-physical result. There are some fundamental boundary conditions that are utilized to almost every domain. Inlet, outlet, wall and symmetry boundary conditions are some of these frequently used boundary conditions. In addition to these, some special boundary conditions should also be constituted to model some certain effects, which influence the domain unlike known boundary conditions. For example, the liquid- vapor interface in a heat pipe needs a special treatment since none of the existent boundary conditions can explain the physical phenomena at this particular region. The effects of boundaries are included into the source terms in the discretized equations. In this chapter, all of the boundary conditions that are employed to the domain shown in Figure 2.1 shall be represented with their numerical implementations to the computer code developed in MATLAB.

## 5.1. Inlet Boundary Conditions

Since energy equation is also solved in addition to the momentum equations, inlet boundary conditions should be specified for both velocity and temperature distributions. The studied domain is illustrated in Figure 5.1. There exist two velocity inlets boundaries, one being the vapor flow inlet and the other being the liquid flow inlet and in addition to those, there is one temperature inlet boundary condition. The velocity inlet boundary conditions are specified at the wick-vapor interface whereas the temperature inlet is given for the boundary nodes at the edge through which the heat input is given as may also be seen in the figure.

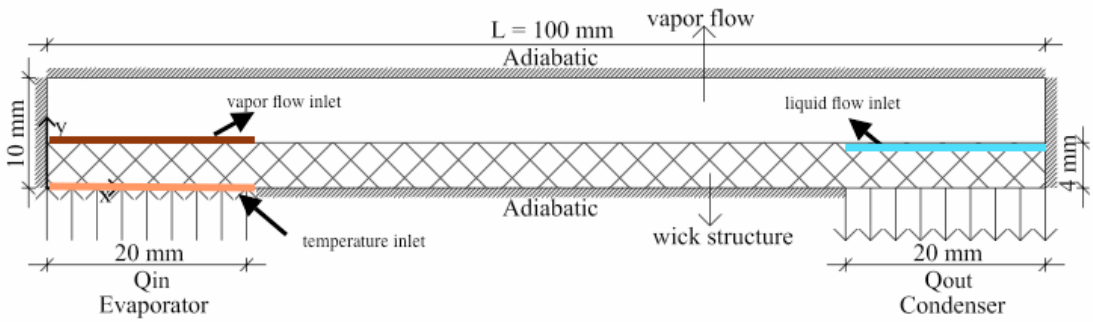


Figure 5.1. Schematic diagram of the domain with inlet boundary conditions

Both velocity and temperature inlet boundary conditions are derived from the energy balance at those boundaries. One fact should be stated here. Since the velocity inlet and outlet boundaries intersect at the liquid-vapor interface, the outlet mass flow rate of the liquid flow in the wick turns out to be the inlet mass flow rate of the vapor flow. Similarly, the mass flow out from the vapor region creates a mass flow inlet to the liquid flow. However, the mass flux should be conserved while this inlet-outlet interaction is formed and since the density values of vapor and liquid are not equal, the velocity values shall not be equal, either. The values of velocity inlet for both vapor and liquid region and temperature inlet at the outer surface can be found by applying energy balance at the liquid vapor interface.

$$q_{in} = q_{conv.} + q_{cond.} + q_s \tag{5.1}$$

Due to the energy balance at the interface, the inlet heat flux is equal to the summation of convective, conductive heat flux values and the heat removed by the evaporation process. These heat flux values and the heat removal from the interface can be calculated by using the following expressions.

$$q_{conv} = \rho_v v_{in} c_{P,v} T_{\text{int}} \tag{5.2}$$

$$q_{cond.} = -k_v \frac{\partial T_v}{\partial y} \tag{5.3}$$

$$q_s = \rho_v v_{in} h_{fg} \tag{5.4}$$

When equations (5.2), (5.3) and (5.4) are substituted in equation (5.1), the inlet velocity in y-direction is obtained.

$$v_{inlet} = \frac{q_{in} + k_v \dfrac{\partial T_v}{\partial y}}{\rho_v (h_{fg} + c_{P,v}.T_{\text{int}})} \tag{5.5}$$

If the temperature gradient is calculated between the liquid vapor interface and the face where the heat flux is applied, the inlet temperature can be evaluated by using equation (5.6).

$$T_{inlet} = T_{\text{int}} + \frac{\left(q_{in} - \rho_{liq}.v_{liq}.T_{\text{int}}.c_{P,liq}\right)\Delta y}{k_{eff}} \tag{5.6}$$

$T_{int}$ in equations (5.2), (5.5) and (5.6) is the temperature value at the wick-vapor interface. The temperature value at the interface is assumed to be at local saturation temperature. Furthermore, the inlet velocity in x-direction is assumed to be zero.

$$u_{inlet} = 0 \tag{5.7}$$

At the inlet nodes whose velocity and temperature values are known, there is no need to solve any momentum or the energy equation. Thus, the equations are solved starting from the internal nodes, which are shaded in the figures below. Besides, the coefficient of the first internal node's neighbor in the direction of inlet boundary is set to zero in the discretized momentum equation. For example, the velocity and temperature inlets of vapor flow is shown in Figures 5.1, 5.2 and 5.4. The south coefficients of the shaded cells should be zero (i.e. $a_S = 0$) since the effect of the boundaries are included into the source term, b. Additionally, the appropriate coefficient should be zero also in pressure correction equation of the shaded cell as indicated in Figure 5.3. Furthermore, no guessed velocity and temperature values are needed at the inlet boundaries due to the fact that they are already known. Therefore, the inlet velocity values and inlet temperature values are directly assigned to the starred values (i.e. $\Phi_S^* = \Phi_S$) during the calculations.

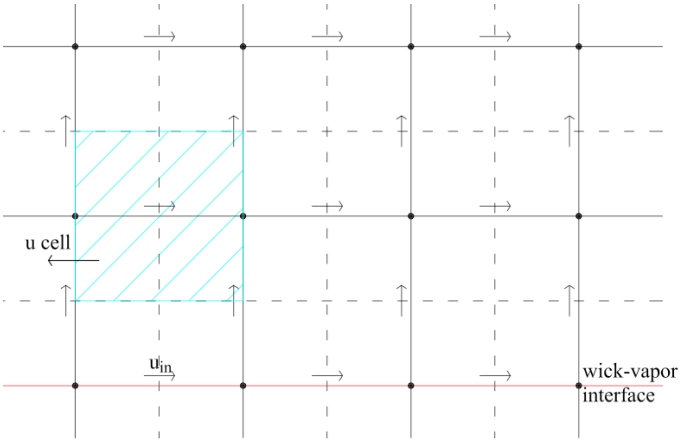


Figure 5.2. The u-velocity node for inlet boundary condition

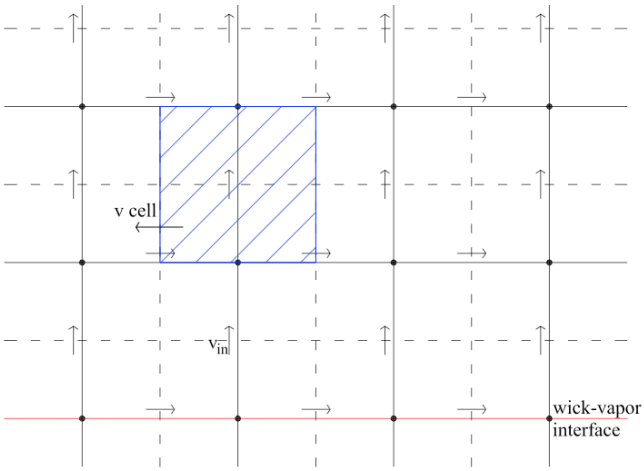


Figure 5.3. The v-velocity node for inlet boundary condition

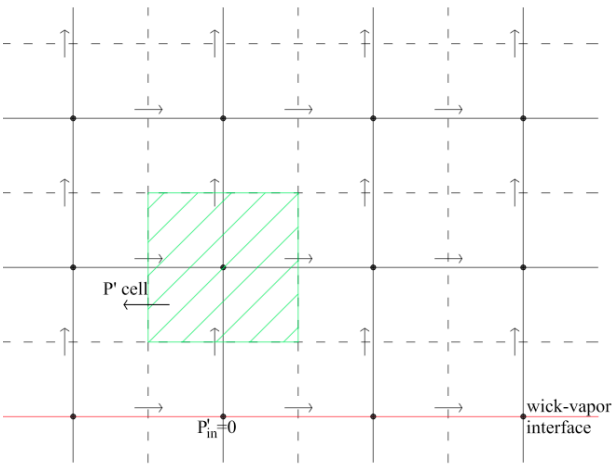


Figure 5.4. The pressure correction node for inlet boundary condition

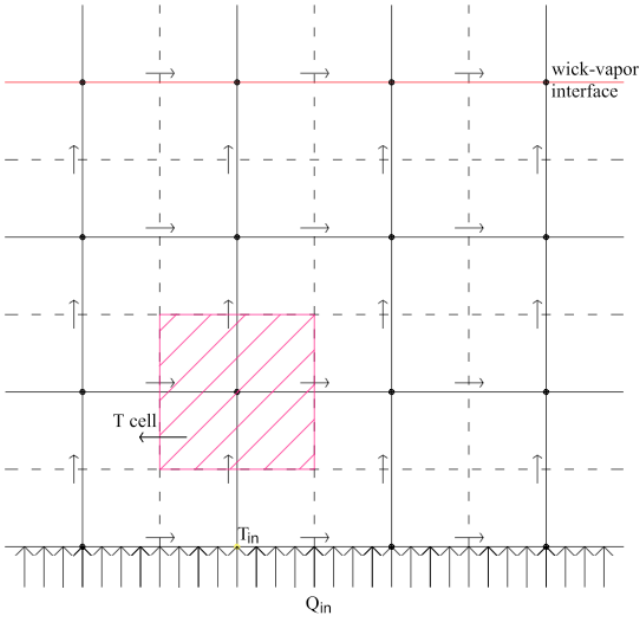

Figure 5.5. The temperature node for inlet boundary condition

## 5.2. Outlet Boundary Conditions

In this study, the outlet boundary conditions are somewhat different than the outlet boundary conditions introduced in most of the references for numerical methods. In most references, the outlet boundary is selected far away from the disturbances and no change occurs in the flow direction nearby the outlet boundary. In such a case, the gradients of all variables are set to zero at the outlet region. However, the outlet boundaries in this study are extremely affected by the disturbances and the direction of the flow changes in the vicinity of outlet boundaries due to the nature of the flow in a heat pipe so alternative boundary conditions should be proposed.

The velocity values are determined by utilizing the conservation of mass between inlet of vapor region and outlet of wick structure as mentioned above. Thus, the velocity outlet for the liquid flow can be obtained by using the following expression.

$$\rho_{liquid} v_{outlet,liquid} A = \rho_{vapor} v_{inlet,vapor} A \tag{5.8}$$

Similarly, the velocity outlet of the vapor flow is also evaluated by employing the conservation of mass at the wick-vapor interface.

Likewise, the outlet boundary for temperature is also found in conjunction with the inlet boundary condition. The only difference is that the heat flux is in the opposite direction of the inlet heat flux. Thus, outlet temperature can be stated as:

$$T_{outlet} = T_{\text{int}} + \frac{\left(-q_{in} - \rho.v_{liq}.T_{\text{int}}.c_P\right)A}{k} \tag{5.9}$$

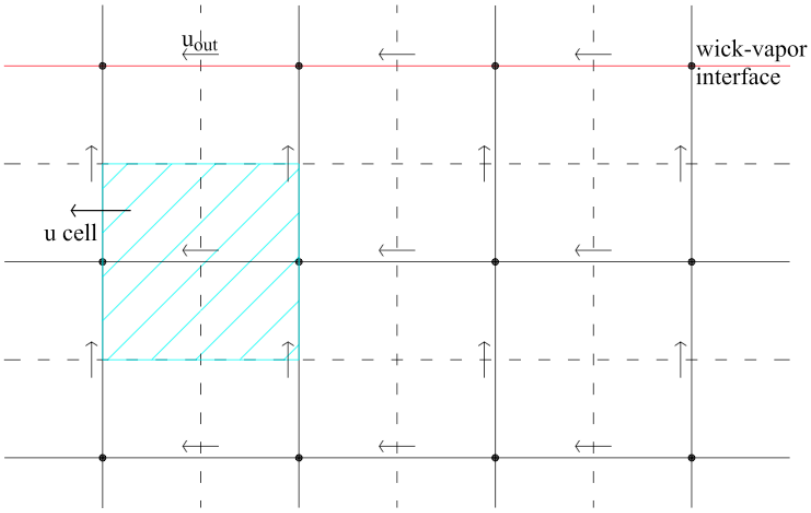


Figure 5.6. The u-velocity node for outlet boundary condition

As the dependent variables at the outlet region are known, there is no need to solve momentum and energy equations for those nodes. The shaded cells in Figures 5.5-5.8 are the last calculated cells of the liquid flow. Hence, their coefficients corresponding to the outlet boundaries are set to zero in the discretized equations (i.e. $a_N = 0$ for velocity and pressure equations, $a_S = 0$ for temperature equation) but the effects of outlet boundaries are included in the source term, b. It should also be noted that the values at the outlet boundaries are known. Therefore, the known outlet variables are directly assigned to starred values (i.e. $\Phi_N^* = \Phi_N$ for velocities and $\Phi_S^* = \Phi_S$ for temperature).

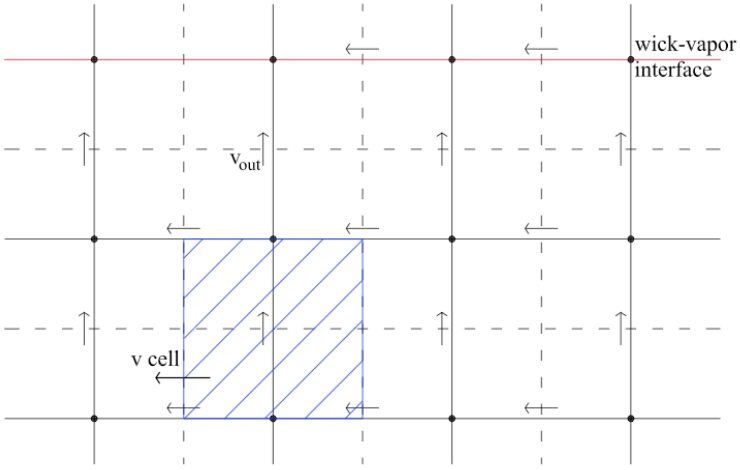


Figure 5.7. The v-velocity node for outlet boundary condition

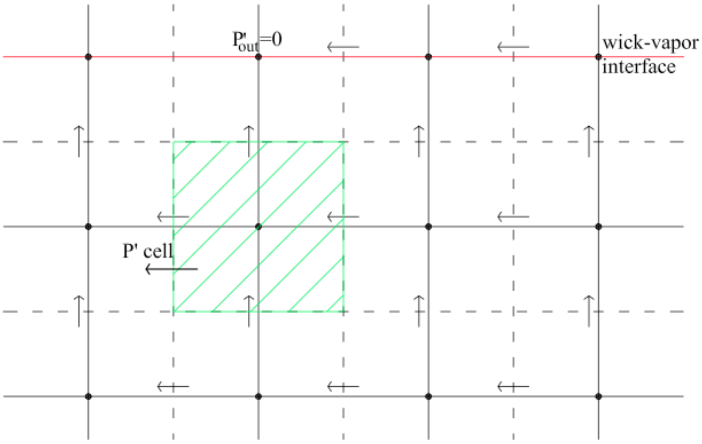


Figure 5.8. The pressure correction node for outlet boundary condition

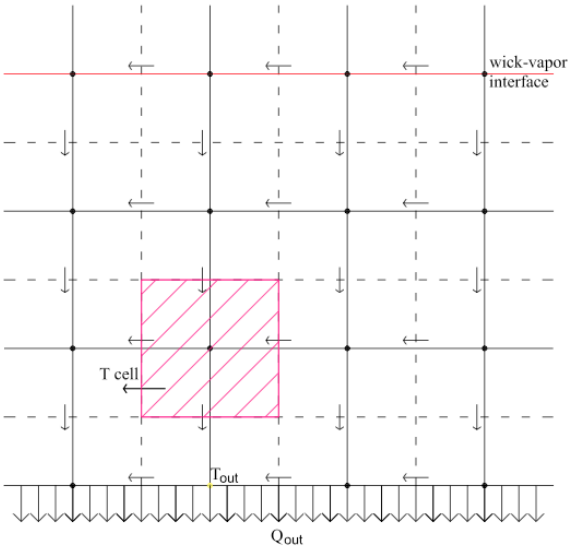


Figure 5.9. The temperature node for outlet boundary condition

## 5.3. Wall Boundary Conditions

There are two types of wall boundary conditions, one of which is the no-slip boundary condition that is implemented to velocity nodes at solid walls and the other is the adiabatic wall boundary condition employed to temperature nodes at solid walls.

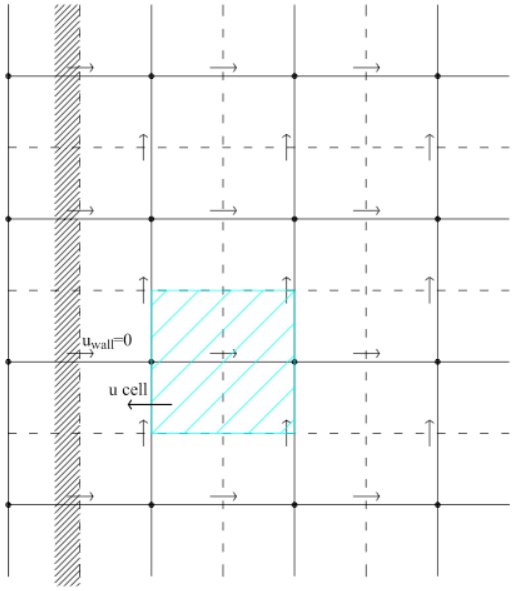


Figure 5.10. The u-velocity node for the wall boundary condition

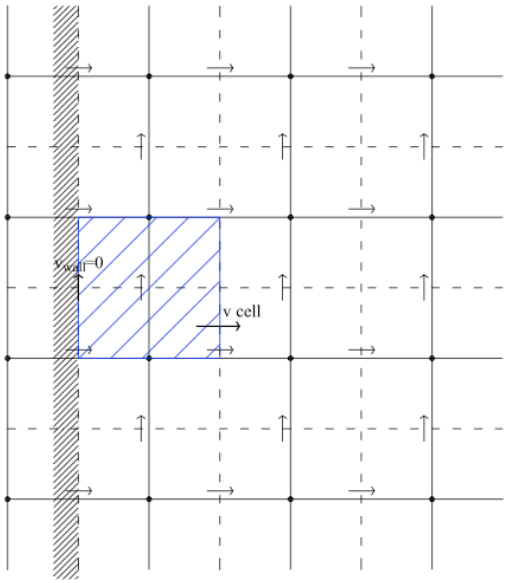


Figure 5.11. The v-velocity node for wall boundary condition

The no-slip boundary condition proposes that the velocity values at the solid walls are equal to zero as shown in Figures 5.9 and 5.10. That is why the appropriate

coefficients in the discretized momentum equations are set to zero (i.e. $a_W = 0$). However, as seen in the above figures, there is a u-velocity cell right on the solid wall while the cell faces of the v-velocity cells intersect the solid wall. Thus, there is no source effect for the u-velocity cells but the shear force at the solid wall has an impact on the values of v-velocity cells. The shaded areas demonstrate the first calculated cells in the vicinity of the solid wall. On the other hand, as seen in Figure 5.11, pressure correction is unnecessary at solid walls and the corresponding coefficients in the discretized pressure correction equation are also set to zero.

The effect of shear force on the v-velocity node can be represented by the expression written below. Note that the wall force is implemented into the source term in the discretized v-velocity equation.

$$S_P = -\frac{\mu}{\Delta x} A \tag{5.10}$$

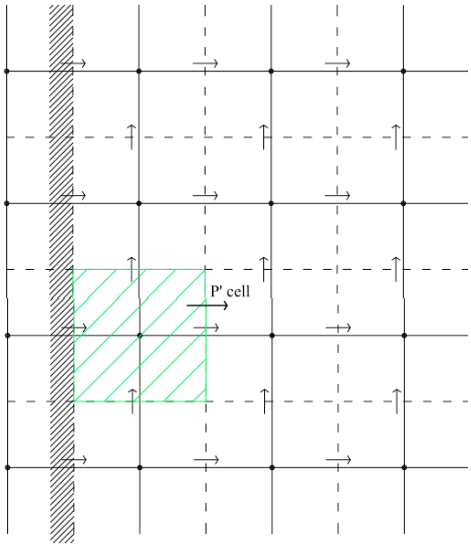


Figure 5.12. The pressure correction node for wall boundary condition

The adiabatic boundary condition is utilized while calculating the temperature at the solid wall. As illustrated in Figure 5.12, there is a temperature node just outside the wall, which is also called a “ghost” cell. According to the adiabatic boundary condition, there is no heat flux through the solid wall. Therefore, $T_1$ and $T_2$ in the figure below should be equal to each other by applying Fourier’s law of thermal conduction at the solid wall. Moreover, the appropriate coefficient is set to zero in the discretized pressure correction equation.

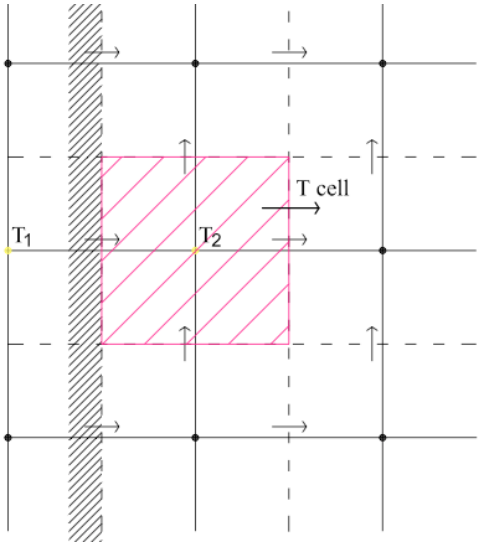

Figure 5.13. The temperature node for wall boundary condition

# CHAPTER 6

# RESULTS AND DISCUSSION

In this study, the results based on the numerical modeling, which was performed for two dimensional flat heat pipe, are presented. The current model assumes no transient change for any values within the iteration process. Thus, the analysis investigates the effects of different variables only for steady state condition. The major results introduced in the scope of this study are the distribution of velocity components along with their profiles at different locations, temperature distribution and pressure drops along the heat pipe as well as its distributions within the domain.

The residuals are strictly monitored during the iteration processes. The residual of a variable is one of the most important aspects in CFD. The importance of the residuals comes from the fact that they can be utilized as an indication to the convergence of the solution.

Before presenting the results obtained in this study, the validity of the computer code are established by comparing the outputs with the existent results examined in different references. However, there are not many references, which perform the modeling with the same method and same boundary conditions utilized in this study. Nevertheless, the results are compared mostly qualitatively rather than quantitatively and it is seen that the trends of the distributions of different variables are mostly consistent with the results of this study. Additionally, the results agree on the order of magnitude in many cases. Yet, it is still necessary to perform quantitative comparison.

## 6.1. Code Validation

The code validation is performed by using the data from Ranjan et al. (2010). The schematic diagram of the investigated flat heat pipe in their work is presented below in Figure 6.1. As can be seen from the figure that the flat heat pipe has one evaporator through which the heat flux is applied and one condenser to release the heat to the ambient. All other surfaces are assumed to be adiabatic solid wall. The heat pipe is composed of copper wall and screen type wick structure, which creates capillary

pressure used to carry the condensed fluid back to the evaporator. Furthermore, the convective boundary condition is applied to the condenser section. The modeling is carried out in two-dimensional space. Water is used as the working fluid. Thermo physical properties of water and copper at 298K are employed in the calculations.

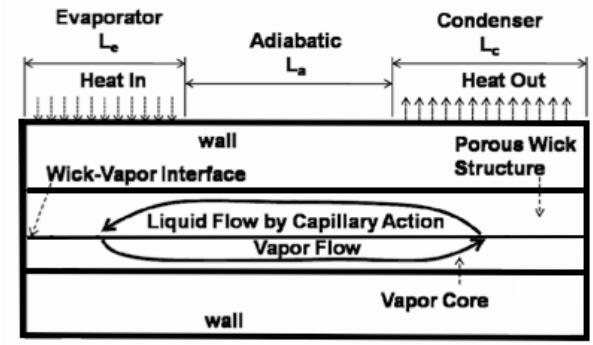


Figure 6.1. Schematic diagram of the flat heat pipe
(Source: Ranjan et al., 2010)

The length and width of the heat pipe are 84mm and 5.1 mm, respectively. Furthermore, the thicknesses of the solid walls on both sides are 1.3mm each while the vapor region has a thickness of 1mm and the wick region covers a thickness of 1.5mm. The length of 19 mm is chosen for evaporator and the condenser length is 32mm. Moreover, a porosity value of 0.56, a permeability value of 1.43 $10^{-11}$ $m^2$ are used and the effective thermal conductivity is taken as 3 W/mK. The heat input given to the evaporator section is 0.5 $W/cm^2$.

The analysis, whose properties are given above, is performed by using the software FLUENT, which is a commercial CFD program. However, an in-house code is developed in the scope of this study. That is why; the in-house code is modified by using the above dimension and thermo physical properties. The results obtained by the in-house code written in MATLAB are found to be consistent with the results of the analysis used for validation.

Figure 6.2 shows the temperature distribution, which is found in the numerical analysis performed by commercial CFD code. The temperature ranges from 290K to 293.5K within the heat pipe with a heat flux of 0.5 $W/cm^2$. As can be derived from the figure that the heat flux is applied to the heat pipe from the upper side, which is colored by red and temperature value is around 293.5K in that part of the heat pipe. Moreover, the region with blue color is the condenser section. The rest of the heat pipe is found to be in thermal equilibrium as shown with green color.

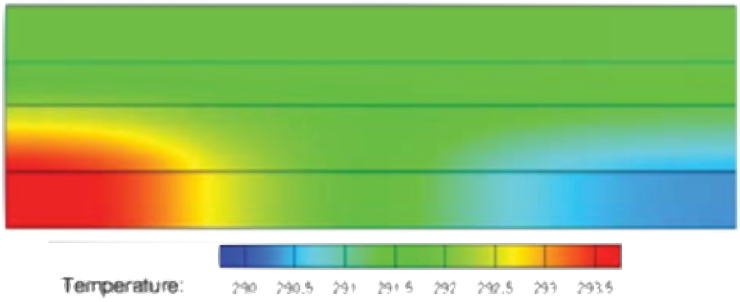


Figure 6.2. Temperature distribution of the flat heat pipe
(Source: Ranjan et al., 2010)

On the other hand, Figure 6.3 is obtained by the MATLAB code developed in the scope of this study. Unlike the above figure, the evaporator and condenser are on the bottom side of the heat pipe. The temperature varies between 293K and 290,5K inside the heat pipe with a heat flux of 0.5 W/cm$^2$. As Figures 6.2 and 6.3 are compared, the temperature distributions found by either method seem to be highly consistent.

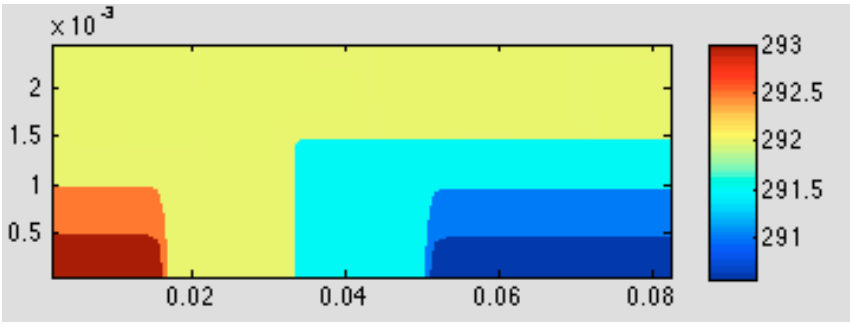


Figure 6.3. Temperature distribution obtained by the in-house code

Furthermore, the pressure drops in both vapor core and wick structure calculated by the MATLAB code is presented in Figure 6.4. As illustrated in the figure, the vapor pressure loss within the heat pipe along the x-direction is found to be 11 Pa while the liquid pressure loss of 62 Pa is calculated in the wick region. Summation of these losses yields the minimum pressure that should be supplied by the capillary force in order to maintain the heat transfer. The pressure distribution trends shown in Figure 6.4 are just the same for all conventional heat pipes as can also be supported by Figure 1.2. Additionally, the quantitative results of the figure below show a very good agreement with the results obtained by (Ranjan et al., 2010). In their study, the vapor and liquid pressure losses are calculated to be 11.6 Pa and 55 Pa, respectively which deviate from the result of present study at a degree of 5.17 % and 11.3 %.

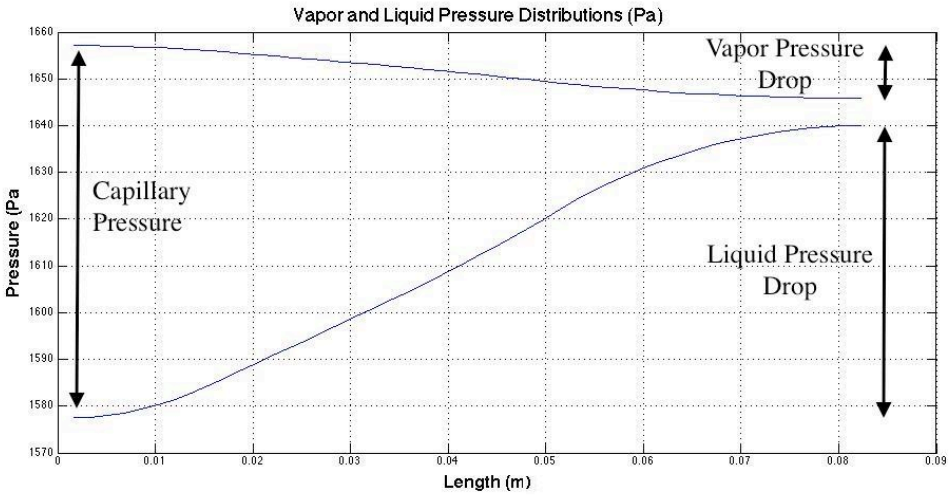


Figure 6.4. Pressure distribution obtained by this study

The maximum liquid and vapor velocity values calculated by the in-house code show also consistency with the results of the commercial code. A maximum liquid velocity is calculated to be $1.78 \times 10^{-5}$ m/s and maximum vapor velocity of 2.97 m/s is obtained by the in-house code while these values are found as 1.8x10-5 m/s and 3 m/s by the commercial code used in the work of Ranjan et al. (2010).

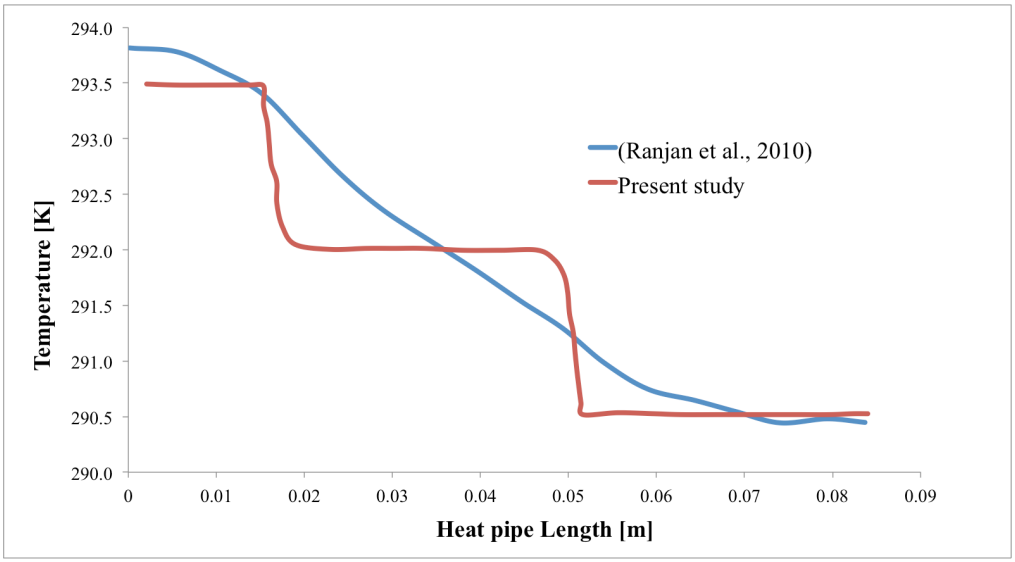


Figure 6.5. Temperature comparison along the heat pipe length

Above, the temperature distributions along the heat pipe length are presented in Figure 6.5. As can be seen in the figure that the trends of these distributions do not match exactly. One fact should be mention at this point, tough. In the scope of this study, the heat pipe wall is not included in the calculations. Thus, the effects of axial conduction in the heat pipe wall are neglected and uniform heat flux inlet and outlet

boundary conditions are assumed for the evaporator and condenser sections, respectively. On the other hand, in the work done by Ranjan et al. (2010), the heat pipe wall is included into the domain and the axial conduction in the heat pipe wall is also considered while evaluating the temperature distribution along the heat pipe. With the inclusion of the wall conduction to the analysis, the temperatures of evaporator and condenser sections effect the whole distribution and this results in a more curved temperature profile as also seen in the above figure. Therefore, relatively different temperature distribution trends are observed even though the temperature drops are consistent in both models.

In conclusion, despite the fact that the two models investigated above have some deviations at certain cases, a general consistency in the results are obtained by making use of different CFD solvers.

In addition to the validation by using the existent studies in literature, analytical comparison is also performed for the vapor core by using the values calculated by the Poiseuille flow approximation. The approximation should be valid in the domain for Re<10 as proposed by the study performed by Ooijen and Hoogendoorn (1979). For this purpose, the calculated velocity profile in the middle section of the vapor core is compared with the velocity profile evaluated by the Poiseuille flow approximation as shown in equation (6.1). In the equation "y" represents the location in y-direction while "h" is the thickness of the vapor core.

$$u(y) = -\frac{h^2}{2\mu}\frac{dP}{dx}\left[\left(\frac{y}{h}\right)-\left(\frac{y}{h}\right)^2\right] \tag{6.1}$$

Figure 6.6 visualizes the results found by each method and as can be derived from the figure that distributions are observed to be highly consistent. Note that the Poiseuille flow approximation should be applied only to vapor core since the wick region is represented by porous medium and some addition forces act on the flow in this region.

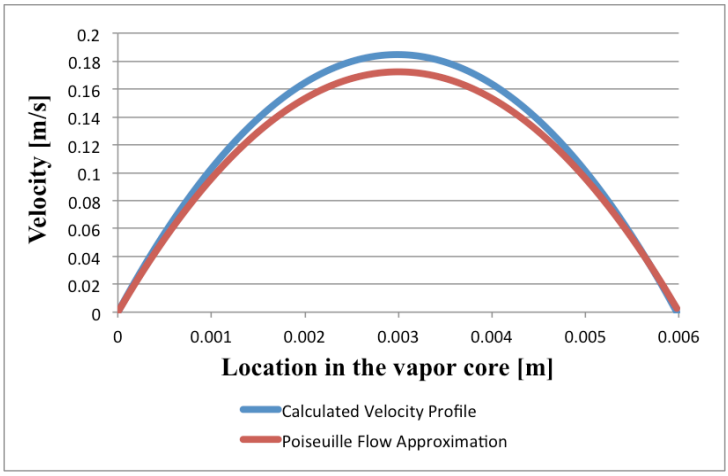


Figure 6.6. Comparison of vapor core velocity and Poiseuille flow approximation in the middle location of vapor core

## 6.2. Grid Independency

In order to prove that the number of mesh is satisfactory to obtain reliable results, a grid independency analysis is performed. For this purpose, the domain is divided into 60x20, 90x30, 120x40, 150x50, 180x60 and 240x80 nodes, in sequence. The iteration processes continue until the mass residuals reach $10^{-9}$ for each number of meshes. It was observed that as the number of nodes in the domain is increased, the computational time increases dramatically. Hence, there occurs a trade off between accuracy of results and computational time. That is why; an analysis is made to choose domain with enough number of nodes, which gives reasonable results in the shortest time period.

It was observed that between 180x60 nodes and 240x80 nodes, the results do not show too much of deviation. This fact can also be seen in Figure 6.7, which shows the maximum u-velocity values obtained by dividing the domain into different numbers of nodes. The temperature values at the end caps show a difference less than 1% and so does maximum vapor velocities. Furthermore, liquid pressure values at the end caps deviate from each other at a degree of 3%. Surprisingly, the maximum liquid velocity values show a difference of 15% but the liquid velocity values are in the order of $10^{-5}$ so that much of deviation is very likely in such a low order of magnitude. On the other hand, the computational time for 240x80 nodes is almost twice the time necessary for 180x60 nodes.

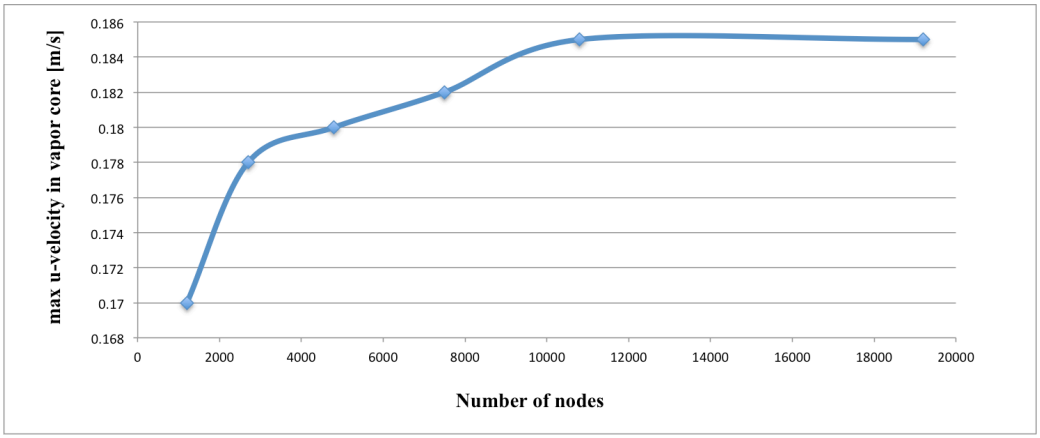

Figure 6.7. Maximum u-velocity values for varying number of nodes

Additionally, the aspect ratio of a single node is also examined because it is observed that inappropriate values of aspect ratio may cause unrealistic results in the analyses. Node aspect ratio is defined to be the ratio of a single node's length to its height. Results show that if the node aspect ratio exceeds 5, unrealistic velocity distributions are obtained for a heat pipe with varying dimensions and number of nodes. On the other hand, the number of nodes in y-direction should not be so small in order to reach the satisfying aspect ratio. Otherwise, incorrect distributions may be obtained due to the small number of nodes in that direction.

All in all, a mesh size of 180x60 with a node aspect ratio of 3.3 is concluded to be sufficient to obtain reliable results in the shortest time period possible. Hence, the presented results below are obtained for 180x60 mesh size.

## 6.3. Results

Now that the mesh independence is performed and the code is validated by using the existing data in the literature, the results obtained by the current work can be presented. The outputs investigated in this study are mainly, the velocity distributions for u-velocity and v-velocity components, the pressure and temperature distributions within the domain and at some certain locations. Furthermore, the velocity vectors are also demonstrated in order to give a visual hint about the magnitude and direction of the velocity components.

The schematic diagram of the heat pipe with physical dimensions and the thermo-physical properties of water and copper are introduced in Chapter 2. A heat flux of $1 W/cm^2$ is applied to the heat pipe through evaporator section and the below results

are obtain. The iteration process continues until continuity residual becomes $10^{-9}$. The convergence is reached after 457 iterations, which last 504 seconds. It can be seen from Figure 6.8 that the residuals of u-momentum, v-momentum, continuity and energy equation reach down to $10^{-6}$, $10^{-8}$, $10^{-9}$ and $10^{-5}$, respectively.

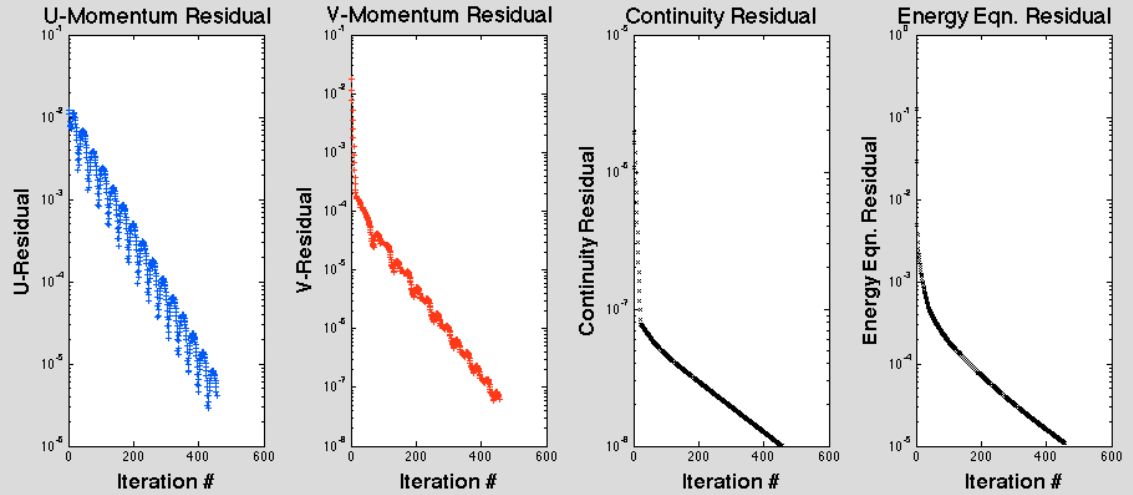


Figure 6.8. Residual values with respect to iteration number

Figure 6.9 illustrates the pressure contour within the heat pipe. The pressure drops for liquid regions is clearly seen in this figure. On the other hand, the drop in vapor core is relatively small compared to the pressure drop in liquid region. That is why it cannot be recognized in the pressure contour. Yet, both vapor and liquid pressure decreases in the flow direction. In other words, while vapor pressure drops towards the condenser section, the liquid pressure drop occurs in the direction towards evaporator section. It can also be derived from the figure that the pressure at the condenser section is found to be almost uniform as expected. This fact is also shown in Figure 1.2 within chapter 1. One fact should be noted at this point. In this study, the main concern is the pressure gradients within the heat pipe. Therefore, the pressure values themselves may vary according to the reference pressure value. Nevertheless, the final results are not affected from the reference pressure value since the pressure gradients are utilized to solve the equations.

The results show that the maximum pressure difference, which is around 820 Pa, is calculated in the evaporator section as presumed and the maximum meniscus curvature occurs in this region. Conversely, the minimum pressure difference, which is almost 20 Pa, is obtained in the condenser section and the minimum meniscus curvature level is observed at this point.

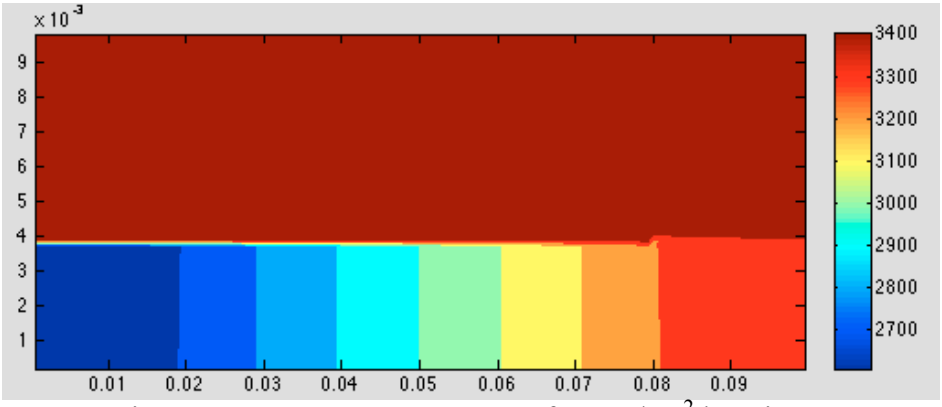


Figure 6.9. Pressure [Pa] contour for 1W/cm$^2$ heat input

A more detailed view into the pressure drops may be found in Figure 6.10. It can be clearly seen that pressure drop in the vapor region is very low since the viscosity of vapor is very low compared to viscosity of liquid. That is why, careful attention should be given to the liquid, thus, to the wick structure in the heat pipe. The pressure values of liquid and vapor phases are almost equal to each other at the condenser end cap, as can also be derived from the figure. Moreover, the below figure also indicates the minimum capillary pressure that should be supplied by the wick structure. The summation of losses within the liquid and vapor regions gives the necessary capillary pressure. For a 1W/cm$^2$ heat input, a capillary pressure of 820 Pa should be supplied by the wick structure. A capillary pressure value lower than 820 Pa results in dry-out condition at the evaporator section since enough liquid cannot be pumped to the evaporator section.

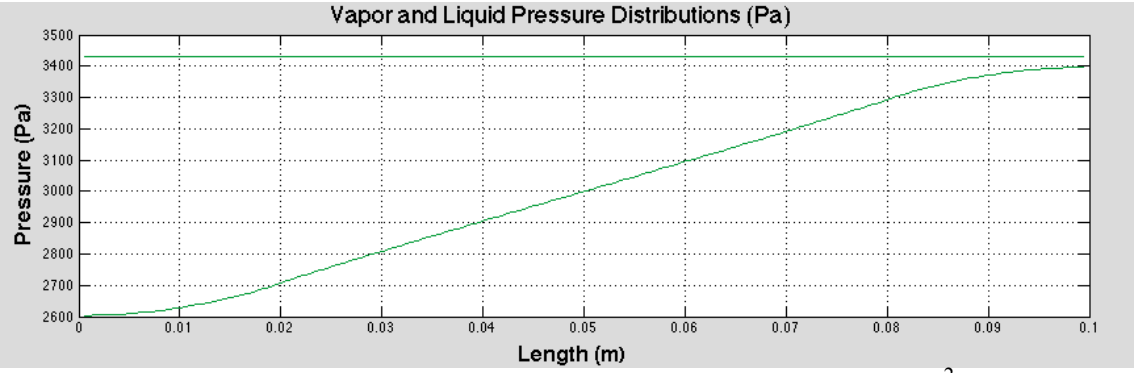


Figure 6.10. Pressure distribution over the heat pipe length for 1W/cm$^2$ heat input

In Figure 6.11, the u-velocity contour inside the heat pipe is presented. Since the u-velocity value of vapor core is $10^2$-$10^3$ times higher than the u-velocity of liquid flow depending on the location, the liquid region in the figure seems to have no velocity. However, the liquid velocity is so small that the variation of it cannot be clearly observed in contour representation.

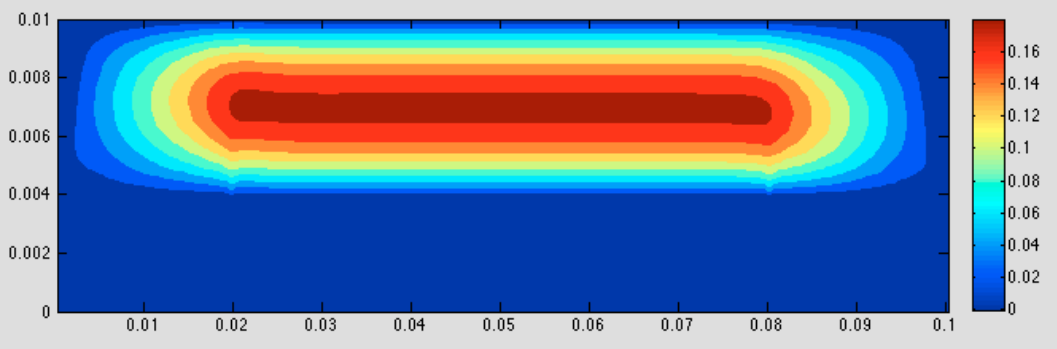


Figure 6.11. U-velocity [m/s] contour for 1W/cm$^2$ heat input

Additionally, the highest velocity value of 0.18 m/s is achieved at the center of vapor core and its value decreases towards the edges because of the frictional force applied by the solid wall. The minimum velocity distribution, on the other hand, is observed in the liquid flow whose maximum value is 1.7x10$^{-5}$ m/s.

In real life conditions, the velocity value at the liquid vapor interface does not equal to zero although it seems to, in the figure. In fact, it may sometimes be so high that the liquid droplets are entrained into the vapor flow because of the force created by the relative velocity of liquid and vapor. However, the interface velocity in the adiabatic region is assumed to be zero in the current study. It is because the interface should be investigated so cautiously that it may be a subject of another study. Hence the zero velocity assumption is decided to be an appropriate simplification for a preliminary analysis.

Similarly, the v-velocity field in contour representation is introduced in Figure 6.12. The velocity inlets and outlet can be easily distinguished at first glance. The evaluation of velocity values at the inlet and outlet boundaries is represented in the previous chapters. The value of velocity inlet to the vapor core is calculated to be 30x10$^{-3}$, while the velocity outlet from the vapor core has the same value as inlet but the opposite direction. Hence, it may be claimed that the mass is conserved throughout the heat pipe.

The magnitude of velocity inside the heat pipe is highly dependent on the heat input and the capillary pressure created by the wick structure. The reason for this dependence comes from the fact that evaporation rate, thus the v-velocity at the interface in the evaporator region, is proportional to the heat input and capillary pressure and as the evaporation rate increases, the velocity within the whole heat pipe rises in order to enhance heat transfer rate. Note that, these parameters can be increased up to some certain levels for a particular heat pipe. One more fact should be mention

here: The vapor velocity in y-direction is higher than the liquid velocity in the same direction due to the density difference and the deviation of velocity values can be clearly seen in the figure.

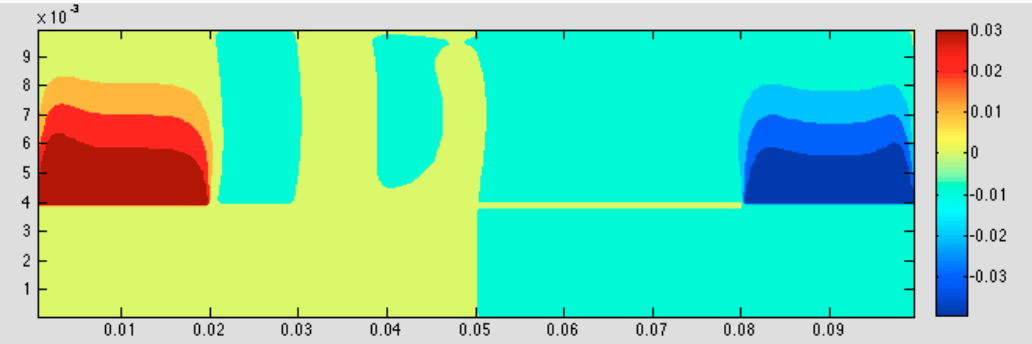


Figure 6.12. V-velocity [m/s] contour for 1W/cm$^2$ heat input

Moreover, Figures 6.13, 6.14 and 6.15 show the velocity vector fields obtained by the current numerical model. The velocity vectors are symbolized with blue arrows. The figures are arranged in the order of flow direction. Hence, Figure 6.13 is presented firstly. The figure illustrates the velocity vectors, which leave the wick region and enter the vapor core.

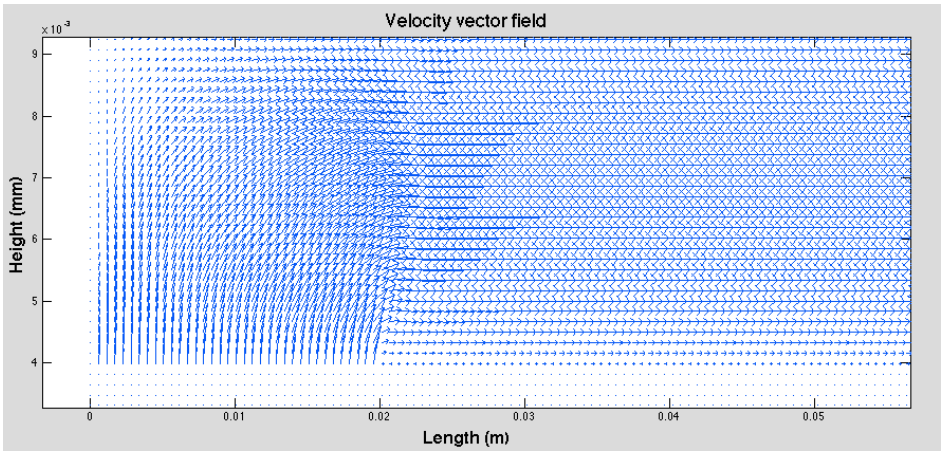


Figure 6.13. Velocity vector field in the vicinity of vapor flow inlet

The velocity vectors then make a turn due to the solid wall boundary conditions and enter the adiabatic section of the vapor core, which is shown in Figure 6.14. In this figure, the order of magnitude of the vapor and liquid velocities can be easily recognized due to the relative lengths of arrows. The lengths of arrows representing the vapor flow are so long that the arrows, which symbolize the liquid flow, cannot be clearly distinguished without zooming.

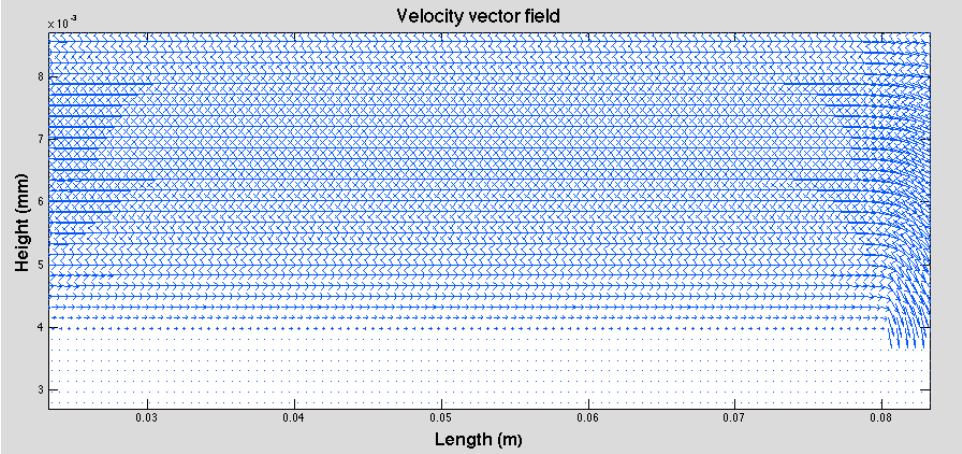

Figure 6.14. Velocity vector field within the adiabatic zone

Finally, Figure 6.15 visualizes the velocity vectors in the condenser section. The velocity vectors reach the condenser section where the flow releases heat and condenses. Here, vectors make another turn and leave the vapor core to enter the wick region.

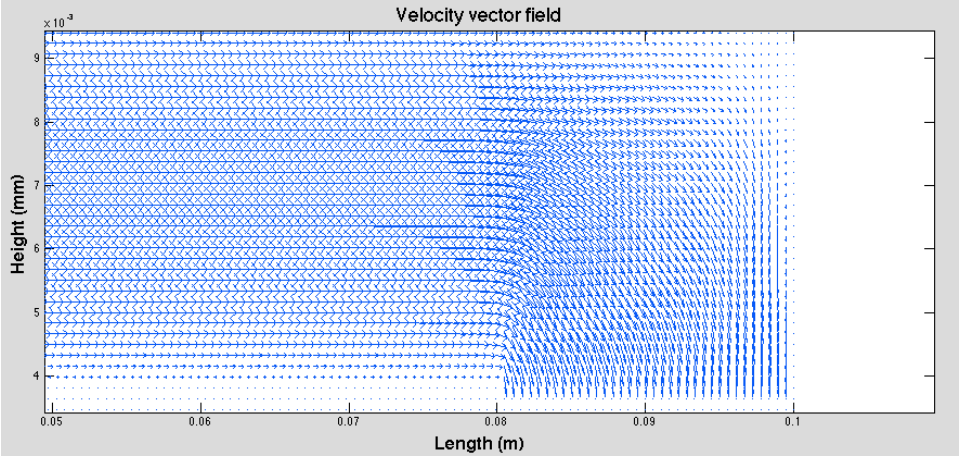

Figure 6.15. Velocity vector field in the vicinity of vapor outlet

After the water vapor is condensed, it is pumped back to the evaporator section where it is evaporated again. This loop maintains without any additional power as long as the operational limitations are not exceed and enough heat is supplied through the evaporator. It should also be mentioned that the maximum Reynolds numbers achieved in the domain are calculated by using the equation (6.2) and they are found to be 6.85 in the vapor core and $9.92 \times 10^{-2}$ for the liquid flow with a the heat input of 1 W/cm$^2$. Therefore, the laminar flow assumption is verified by these numbers.

$$\mathrm{Re} = \frac{\rho u A}{\mu} \tag{6.2}$$

In Figure 6.16, velocity vectors in different locations within the heat pipe are presented for better understanding. The velocity profiles show parabolic trends in the middle section due to the wall boundary conditions. These types of trends are expected for fully developed flows. On the other hand, for inlet and outlet regions the vectors tend to change directions due to the blowing and suction boundaries.

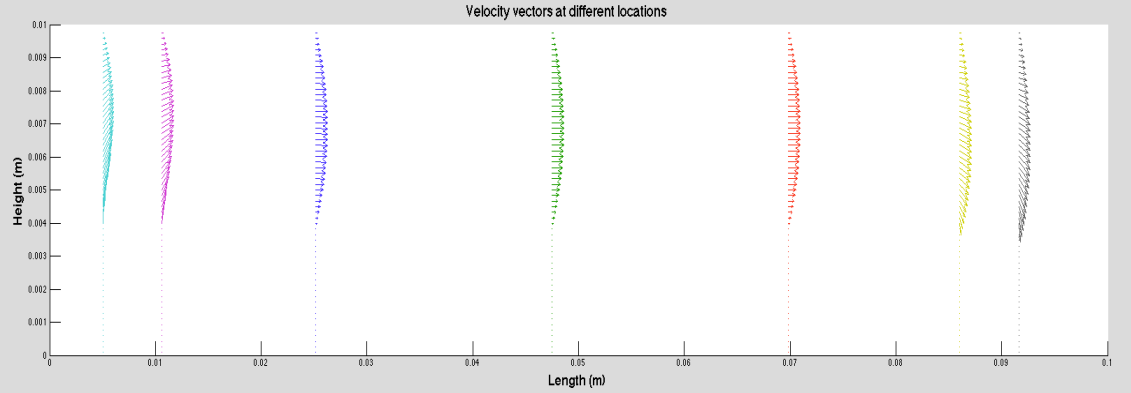


Figure 6.16. Velocity vectors at different locations for 1W/cm$^2$ heat input

Last but not least, the temperature contour is presented in Figure 6.17. The evaporator and condenser sections can be easily distinguished. The highest temperature difference of 0.2K is achieved within the heat pipe as can also be seen in the color bar placed next to the temperature field.

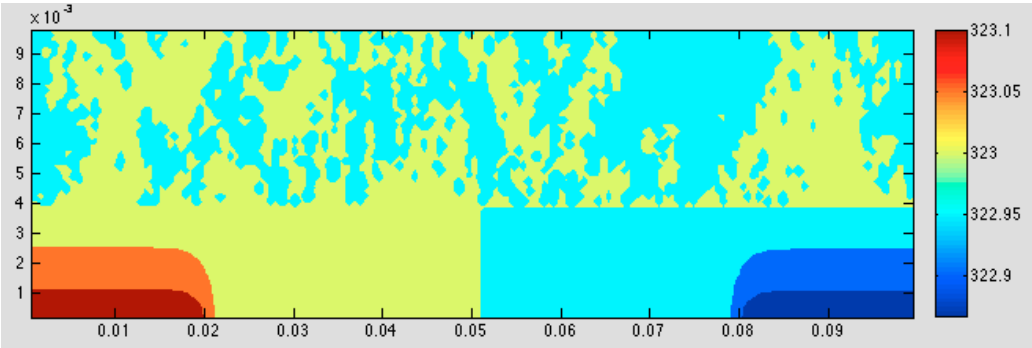


Figure 6.17. Temperature [K] contour for 1W/cm$^2$ heat input

The highest temperature, which is of 323.1 K, is achieved in the evaporator section. On the other hand, the lowest temperature value of 322.9 K is observed in the condenser section. Additionally, the vapor core shows an almost adiabatic characteristic

as expected and its temperature value stays constant at 323K. Even though there are some fluctuations in the temperature values in that region, this problem can be overcome by increasing the number of iterations, thus decreasing the value of convergence criterion further. Moreover, the temperature of the section between the evaporator and condenser regions in the wick structure shows a constant temperature profile as predicted. Therefore, this section is called the adiabatic section. The adiabatic section can be clearly seen in Figure 6.18, which shows the temperature distribution along the outside boundary of the wick structure. The assumption that the evaporation and condensation occur only in evaporator and condenser zone, can be distinctly observed in the below figure. Additionally, there are smooth temperature transitions between the regions at the outside boundary of wick structure as can also be seen in the figure.

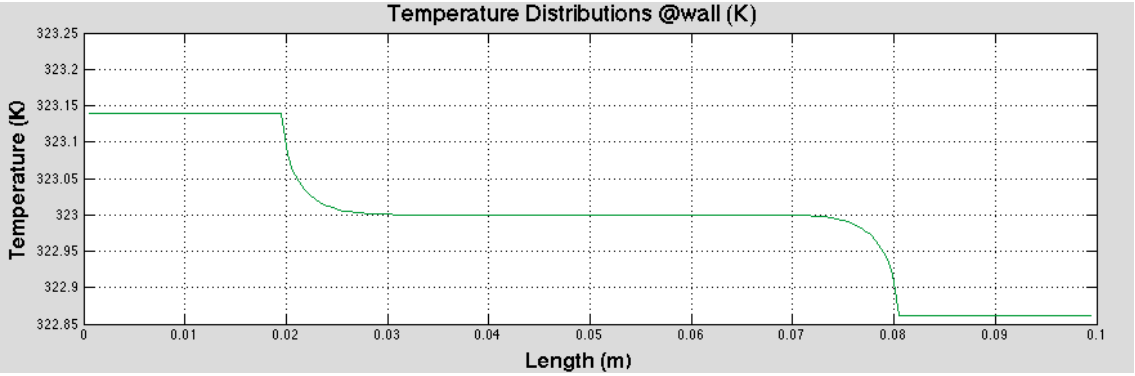


Figure 6.18. Temperature distribution over the heat pipe length

In addition to the temperature distribution in the domain, the heat flux values at both bottom and top surfaces are also calculated. The results indicate that there is no heat flux at the top surface and the adiabatic region of the bottom surface. However, there is an inlet heat flux of $1x10^4$ in the evaporator section and there is an outlet heat flux of the same amount illustrated in Figure 6.19.

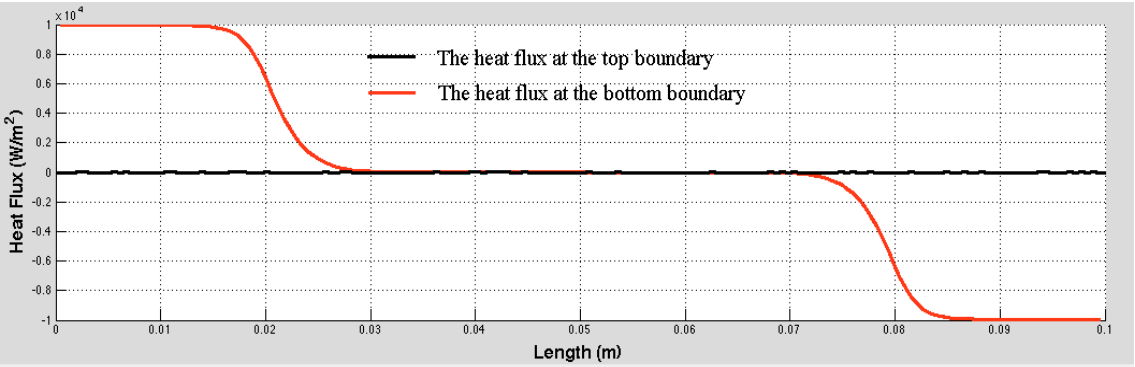


Figure 6.19. Heat flux values at the top and bottom boundary

One of the main purposes of this study is to investigate the effects of heat input on the capillary pressure required for proper heat transport. With regard to this aim, Figure 6.20 visualizes results of parametric analysis performed on the pressure losses in both vapor and liquid flows along the heat pipe length for different heat inputs. The summation of pressure losses within the heat pipe gives the capillary pressure needed to operate the heat pipe properly. In the figure given below, the pressure difference for each color at the zero x-location gives the capillary pressure needed for that much of heat input. For example, around 170 Pa of capillary pressure is required for 0.3 W/cm$^2$ of heat input. As the heat input is increased, the evaporation rate elevates so does the condensation rate due to the faster mass transport from evaporator to condenser. Thus, a higher amount of condensed liquid is obtained in the condenser, which needs a better pumping force in order to supply enough condensate to prevent evaporator dry-out. That is why; a larger capillary pressure is required for higher heat inputs.

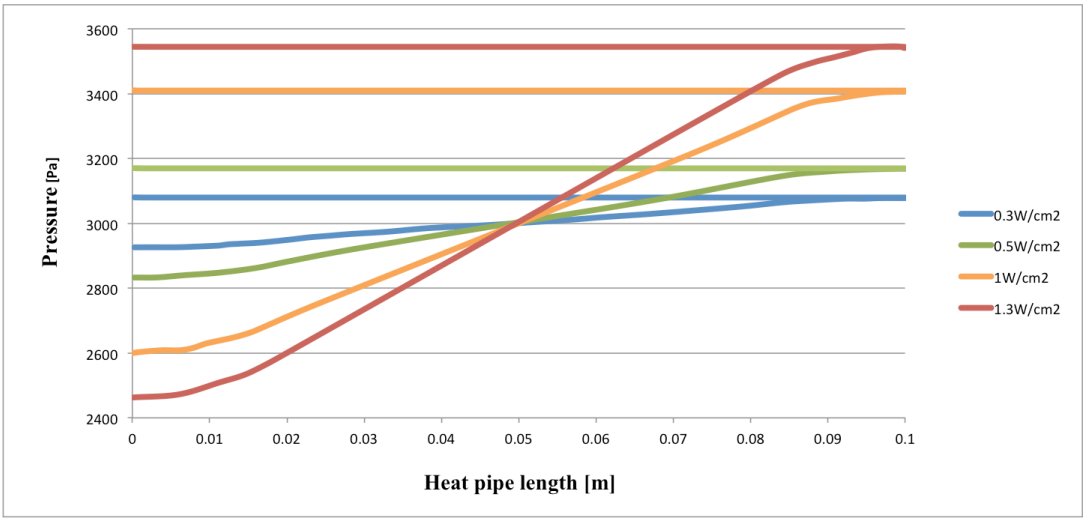


Figure 6.20. Pressure distribution along the heat pipe length for various heat inputs

In addition to the parametric analysis performed by changing the heat input given to the heat pipe, another study is carried out by increasing ratio of the heat pipe length to the heat pipe height. The results are obtained by utilizing a heat input of 1 $W/cm^2$ to the heat pipe and all other parameters are kept constant except the heat pipe length. The effect of different heat pipe length to heat pipe height, which are quantitatively 10, 30, 50, 70 and 100, on the required capillary pressure is examined. Figure 6.21 illustrates the results evaluated in the analysis. The results show that the pressure losses, thus the required capillary pressure values, within the heat pipe is proportional to heat pipe aspect ratio so it increases with elevated heat pipe aspect ratio as expected. The reason for such a trend comes from the fact that the vapor and liquid flow experiences more disturbances within the vapor core and wick region, respectively as the length of the heat pipe is increased. Therefore, the wick structure, which supplies the necessary capillary pressure, should be constructed accordingly.

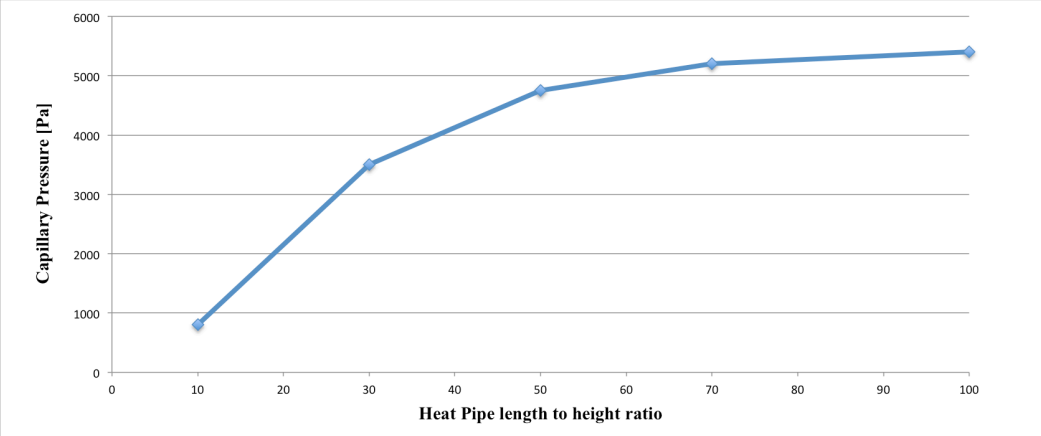


Figure 6.21. Required capillary pressure values for varying heat pipe aspect ratio

Furthermore, as the heat input is increased, the operational pressure, thus the operational temperature, of the heat pipe also increase. Consequently, some of the operational limitation of the heat pipe can be exceeded. Therefore, pressure distribution within the heat pipe plays a very important role on determination of the heat pipe operational characteristics and the results of this study can be utilized for this very reason.

# CHAPTER 7

# CONCLUSION

In the scope of this study, a MATLAB code is developed to model a flat heat pipe in two-dimensional space by utilizing numerical methods. Asymmetric boundary conditions are applied to the heat pipe. Vapor and wick regions are incorporated in the analysis and governing equations are solved under steady state, subsonic, laminar, incompressible and Newtonian flow assumptions. Brinkman-Forchheimer extended Darcy model is employed for the liquid flow in the wick structure. Furthermore, the model accounts for uniform injection and suction in the evaporator and condenser sections and it is assumed that evaporation and condensation only occur in evaporator and condenser sections, respectively. Wick structure is presumed to be isotropic and saturated with working fluid. Besides, the interfacial velocity is found from energy balance at the liquid-vapor interface. All thermo physical properties are taken as constant and no body forces are included in the model.

The governing equations, which are in the form of differential equations, are converted to the algebraic equations by means of finite volume method. The final form of the algebraic equation set is called as the nodal equations. Hybrid differencing scheme is used to calculate the coefficients of the nodal equations. In order to overcome the difficulties caused by the pressure terms in the momentum equations, staggered grid arrangement is applied to the domain along with the SIMPLE algorithm. The major results introduced in this study are the distribution of velocity components along with their profiles at different locations, temperature distribution and pressure drops along the heat pipe as well as its distributions within the domain. Moreover, the effects of heat input and the heat pipe aspect ratio to the required capillary pressure are investigated to determine the operational characteristics of a heat pipe.

The code validation is performed by using the data from the work done by Ranjan et al. (2010). Despite the fact that the current model has some deviations at certain cases, a general consistency in the results is obtained.

Furthermore, a mesh independence analysis is performed to determine the minimum number of nodes and maximum node aspect ratio in order to obtain reliable

results in the shortest time period. It is concluded that 180x60 mesh size with node aspect ratio of 3.3 gives satisfactory results.

The final results indicate that the major pressure loss occurs in the wick structure. The parametric study verifies that total pressure loss increases with the elevated heat input to the heat pipe and increased heat pipe aspect ratio so capillary pressure value should be adjusted accordingly. Additionally, the largest pressure difference is observed in the evaporator section, which results in the highest meniscus curvature in this section. On the other hand, the lowest pressure difference, thus the minimum meniscus curvature, is obtained in the condenser section.

Moreover, the velocity profiles point out that the maximum velocity within the heat pipe is achieved in the vapor core and it is $10^2$-$10^3$ times larger than the velocity of liquid phase in the wick structure. Nevertheless, the laminar flow assumption is fairly satisfied throughout the heat pipe for the given input.

Lastly, temperature profile of the heat pipe and the temperature distribution along the outside boundary of the wick structure are also presented in Chapter 6. According to the temperature contour representation, the highest temperature is reached at the evaporator section while the lowest temperature is obtained in the condenser section, as expected. Moreover, the temperature distribution along heat pipe length legitimates the uniform suction, injection and truly adiabatic section assumption.

In conclusion, the results obtained in this study can be a preliminary advisor for the heat pipe manufacturer. The code developed in the scope of the study is so flexible that any parameter can be adjusted to any scenario and unlike the commercial CFD codes; the user can actually understand the whole process happening behind the software interface, and monitor any additional variable throughout the analyses. Additionally, the different solution methods can be easily adapted to the MATLAB code written and a robust solution can be achieved for any flow modeling.

For the future of the current study; the wick-vapor interface should be investigated more carefully since this region constitutes a phase change process and some effects caused by having a two-phase region cannot be observed due to the simplifications made to model the interface. Furthermore, the ignored interaction between liquid and vapor phases should also be included in the analyses and the effect of entrainment limit to the heat pipe operational characteristics can also be observed.

In the current study, the wick structure is assumed to be fully saturated with working fluid. However, the liquid level at the evaporator section is not constant during

whole process. Hence, more detailed assumptions should be made in the wick structure so that the effects of liquid level at the evaporator section can be investigated. Moreover, in addition to the wick and vapor regions, the solid wall may be incorporated into the calculations and the conduction equation in the solid wall can also be solved. Thus, the effect of wall conduction on the distributions can be detected.

In order to examine the critical regions in a more detailed way, the number of nodes can be increased only at those regions and the node numbers for rest of the domain can remain the same. This way, a dramatic increase in the run time due to higher number of nodes can be avoided.

In this study, the validity of the code is checked by comparing the results with the output of another numerical study. However, for a future work, an experimental study can be conducted and the validation may be performed by comparing the results of numerical study with the experimental work.

Furthermore, different heating and cooling conditions may be applied to the heat pipe to monitor their effects on the heat pipe performance. Additionally, the analysis can be extended to model the heat pipe under transient behavior and; compressible and turbulent flow assumptions.

# REFERENCES


Aghvami, M., & Faghri, A. (2011). Analysis of flat heat pipes with various heating and cooling configurations. *Applied Thermal Engineering, 31*(14-15), 2645-2655. doi: 10.1016/j.applthermaleng.2011.04.034

Chen, Y., Zhang, C., Shi, M., Wu, J., & Peterson, G. P. (2009). Study on flow and heat transfer characteristics of heat pipe with axial "Ω"-shaped microgrooves. *International Journal of Heat and Mass Transfer, 52*(3-4), 636-643. doi: 10.1016/j.ijheatmasstransfer.2008.08.003

Cleary, M., North, M. T., Van Lieshout, M., Brooks, D. A., Grimes, R., & Hodes, M. (2013). Reduced Power Precision Temperature Control Using Variable Conductance Heat Pipes. *IEEE Transactions on Components, Packaging and Manufacturing Technology, 3*(12), 2048-2058. doi: 10.1109/tcpmt.2013.2270286

Faghri, A. (1995). *Heat Pipe Science and Technology*.

Faghri, A. (2012). Review and Advances in Heat Pipe Science and Technology. *Journal of Heat Transfer, 134*(12), 123001. doi: 10.1115/1.4007407

Gaugler, R. S. (1944). U.S. Patent No. 2350348.

Grover, G. M. (1966). U.S. Patent No. 3229759.

Harley, C., & Faghri, A. (1995). Two-Dimensional Rotating Heat Pipe Analysis. *Journal of Heat Transfer, 117*(1), 202. doi: 10.1115/1.2822304

Hung, Y. M., & Tio, K.-K. (2010). Analysis of Microheat Pipes With Axial Conduction in the Solid Wall. *Journal of Heat Transfer, 132*(7), 071301. doi: 10.1115/1.4000947

Hung, Y. M., & Tio, K.-K. (2012). Thermal analysis of optimally designed inclined micro heat pipes with axial solid wall conduction. *International Communications in Heat and Mass Transfer, 39*(8), 1146-1153. doi: 10.1016/j.icheatmasstransfer.2012.07.009

Judge, J. F. (1966). RCA Test Thermal Energy Pipe. *Missiles and Rockets*, 36-38.

Leefer, B. I. (1966). *Nuclear Thermionic Energy Converter*. Paper presented at the 20th Annual Power Sources Conference, Atlantic City.

Ooijen, H. v., & Hoogendoorn, C. J. (1979). Vapor Flow Calculations in a Flat-Plate Heat Pipe. *AIAA Journal, 17*(11), 1251-1259. doi: 10.2514/3.61306

Patankar, S. V. (1980). *Numerical Heat Transfer and Fluid Flow*: Hemisphere Publising Corporation.

Patankar, S. V., & Spalding, D. B. (1972). A calculation procedure for heat, mass and momentum transfer in three-dimensional parabolic flows. *International Journal of Heat and Mass Transfer, 15*(10), 1787-1806. doi: 10.1016/0017-9310(72)90054-3

Perkins, J. (1836). U.K. Patent No. 7059.

Peterson, G. P. (1994). *An Introduction to Heat Pipes: Modelling, Testing and Applications*. New York: Wiley.

Ranjan, R., Murthy, J. Y., Garimella, S. V., & Vadakkan, U. (2010). A numerical model for transport in heat pipes considering wick microstructure effects. 1-10. doi: 10.1109/itherm.2010.5501374

Ranjan, R., Murthy, J. Y., Garimella, S. V., & Vadakkan, U. (2011). A numerical model for transport in flat heat pipes considering wick microstructure effects. *International Journal of Heat and Mass Transfer, 54*(1-3), 153-168. doi: 10.1016/j.ijheatmasstransfer.2010.09.057

Reay, D., & Kew, P. (2006). *Heat Pipes Theory, Design and Applications*: Elsevier.

Shabgard, H., & Faghri, A. (2011). Performance characteristics of cylindrical heat pipes with multiple heat sources. *Applied Thermal Engineering, 31*(16), 3410-3419. doi: 10.1016/j.applthermaleng.2011.06.026

Sobhan, C. B., Garimella, S. V., & Unnikrishnan, V. V. (2000). A computational model for the transient analysis of flat heat pipes. *Itherm 2000: Seventh Intersociety Conference on Thermal and Thermomechanical Phenomena in Electronic Systems, Vol 2, Proceedings*, 106-113. doi: Doi 10.1109/Itherm.2000.866178

T.P., C. (1965). Theory of Heat Pipes. Los Alamos Scientific Laboratory.

Tong, B. Y., Wong, T. N., & Ooi, K. T. (2001). Closed-loop pulsating heat pipe. *Applied Thermal Engineering, 21*(18), 1845-1862. doi: 10.1016/s1359-4311(01)00063-1

Vadakkan, U., Garimella, S. V., & Murthy, J. Y. (2004). Transport in Flat Heat Pipes at High Heat Fluxes From Multiple Discrete Sources. *Journal of Heat Transfer, 126*(3), 347. doi: 10.1115/1.1737773

Vafai, K., & Wang, W. (1992). Analysis of flow and heat transfer characteristics of an asymmetrical flat plate heat pipe. *International Journal of Heat and Mass Transfer, 35*(9), 2087-2099. doi: 10.1016/0017-9310(92)90054-v

Versteeg, H. K., & Malalasekera, W. (2007). *An Introduction to Computational Fluid Dynamics* (Second ed.): Pearson.

Xiao, B., & Faghri, A. (2008). A three-dimensional thermal-fluid analysis of flat heat pipes. *International Journal of Heat and Mass Transfer, 51*(11-12), 3113-3126. doi: 10.1016/j.ijheatmasstransfer.2007.08.023

Zhu, N., & Vafai, K. (1996). The effects of liquid-vapor coupling and non-Darcian transport on asymmetrical disk-shaped heat pipes. *International Journal of Heat and Mass Transfer, 39*(10), 2095-2113. doi: 10.1016/0017-9310(95)00279-0

Zhu, N., & Vafai, K. (1999). Analysis of cylindrical heat pipes incorporating the effects of liquid–vapor coupling and non-Darcian transport—a closed form solution. *International Journal of Heat and Mass Transfer, 42*(18), 3405-3418. doi: 10.1016/s0017-9310(99)00017-4

Zuo, Z. J., & Faghri, A. (1998). A network thermodynamic analysis of the heat pipe. *International Journal of Heat and Mass Transfer, 41*(11), 1473-1484. doi: 10.1016/s0017-9310(97)00220-2